

1 **Bimodal Distribution of Sulfuric Acid Aerosols in the Upper Haze of Venus**

2

3 Peter Gao<sup>1,\*</sup>, Xi Zhang<sup>1,2</sup>, David Crisp<sup>3</sup>, Charles G. Bardeen<sup>4</sup>, and Yuk L. Yung<sup>1</sup>

4

5 *<sup>1</sup>Division of Geological and Planetary Sciences, California Institute of Technology, Pasadena,*  
6 *CA, USA, 91125*

7 *<sup>2</sup>Department of Planetary Sciences and Lunar and Planetary Laboratory, University of Arizona,*  
8 *Tucson, AZ, USA, 85721*

9 *<sup>3</sup>Jet Propulsion Laboratory, California Institute of Technology, Pasadena, CA, USA, 91109*

10 *<sup>4</sup>National Center for Atmospheric Research, Boulder, CO, USA, 80307*

11

12 *\*Corresponding author at: Division of Geological and Planetary Sciences, California Institute of*  
13 *Technology, Pasadena, CA, USA, 91125*

14 *Email address: [pgao@caltech.edu](mailto:pgao@caltech.edu)*

15 *Phone number: 626-298-9098*

16 **Abstract**

17 Observations by the SPICAV/SOIR instruments aboard Venus Express have revealed that the  
18 upper haze (UH) of Venus, between 70 and 90 km, is variable on the order of days and that it is  
19 populated by two particle modes. We use a one-dimensional microphysics and vertical transport  
20 model based on the Community Aerosol and Radiation Model for Atmospheres to evaluate  
21 whether interaction of upwelled cloud particles and sulfuric acid particles nucleated *in situ* on  
22 meteoric dust are able to generate the two observed modes, and whether their observed  
23 variability are due in part to the action of vertical transient winds at the cloud tops. Nucleation of  
24 photochemically produced sulfuric acid onto polysulfur condensation nuclei generates mode 1  
25 cloud droplets, which then diffuse upwards into the UH. Droplets generated in the UH from  
26 nucleation of sulfuric acid onto meteoric dust coagulate with the upwelled cloud particles and  
27 therefore cannot reproduce the observed bimodal size distribution. By comparison, the mass  
28 transport enabled by transient winds at the cloud tops, possibly caused by sustained subsolar  
29 cloud top convection, are able to generate a bimodal size distribution in a time scale consistent  
30 with Venus Express observations. Below the altitude where the cloud particles are generated,  
31 sedimentation and vigorous convection causes the formation of large mode 2 and mode 3  
32 particles in the middle and lower clouds. Evaporation of the particles below the clouds causes a  
33 local sulfuric acid vapor maximum that results in upwelling of sulfuric acid back into the clouds.  
34 In the case where the polysulfur condensation nuclei are small and their production rate is high,  
35 coagulation of small droplets onto larger droplets in the middle cloud may set up an oscillation in  
36 the size modes of the particles such that precipitation of sulfuric acid “rain” may be possible  
37 immediately below the clouds once every few Earth months. Reduction of the polysulfur  
38 condensation nuclei production rate destroys this oscillation and reduces the mode 1 particle  
39 abundance in the middle cloud by two orders of magnitude. However, it better reproduces the  
40 sulfur-to-sulfuric-acid mass ratio in the cloud and haze droplets as constrained by fits to UV  
41 reflectivity data. In general we find satisfactory agreement between our nominal and transient  
42 wind results and observations from Pioneer Venus, Venus Express, and Magellan, though  
43 improvements could be made by incorporating sulfur microphysics.

44

45 *Keywords:* Atmospheres, composition; Atmospheres, structure; Atmospheres, dynamics; Venus;  
46 Venus, atmosphere

## 47 **1. INTRODUCTION**

48 Sulfuric acid aerosols make up most of the global cloud deck and accompanying hazes  
49 that shroud the surface of Venus (Esposito et al. 1983). As a result, the radiation environment and  
50 energy budget at the surface and throughout the atmosphere is strongly affected by the vertical  
51 extent, size distribution, and mean optical properties of these particles. These aerosols also serve  
52 as a reservoir for sulfur and oxygen, and thus play a major part of the global sulfur oxidation  
53 cycle (Mills et al. 2007). Furthermore, recent studies by Zhang et al. (2010; 2012a) have  
54 hypothesized that the upper haze layer could provide the source of sulfur oxides above 90 km.  
55 Therefore, studying aerosols is a crucial step in understanding the climate and chemistry on  
56 Venus.

57 Observations from the Pioneer Venus atmospheric probes (Knollenberg and Hunten  
58 1980) helped constrain the number density and size distribution of the aerosols in the cloud deck,  
59 and revealed the possibility of two size modes with mean radii  $\sim 0.2 \mu\text{m}$  (mode 1) and  $\sim 1 \mu\text{m}$   
60 (mode 2), along with a third, controversial mode with radius  $\sim 3.5 \mu\text{m}$  whose existence has been  
61 challenged (Toon et al. 1984). The clouds were also vertically resolved into three distinct  
62 regions: the upper cloud, from 58 to 70 km; the middle cloud, from 50 to 58 km; and the lower  
63 cloud, from 48 to 50 km. Mode 1 particles have the largest number densities at all altitudes,  
64 while modes 2 and 3 particles are relatively more abundant in the middle and lower clouds than  
65 in the upper cloud (Knollenberg and Hunten 1980). Both entry probe (Knollenberg and Hunten  
66 1980; Esposito et al. 1983) and remote sensing (Crisp et al. 1989; 1991; Carlson et al. 1993;  
67 Grinspoon et al. 1993; Hueso et al. 2008) indicate that the middle and lower clouds are much  
68 more variable than the upper cloud. This variability may be associated with strong convective  
69 activity within the middle cloud, where downdrafts with amplitudes as large as  $3 \text{ m s}^{-1}$  and

70 updrafts as large as  $1 \text{ m s}^{-1}$  were measured *in situ* by the VEGA Balloons (Ingersoll et al. 1987;  
71 Crisp et al. 1990).

72         These observations of the Venus clouds have been interpreted using numerical models  
73 that account for transport and/or aerosol microphysics. Toon et al. (1982) showed that sulfur  
74 could be present in the upper cloud under low oxygen conditions in sufficient amounts to form  
75 mode 1 particles, with mode 2 particles arising from the coagulation of these particles and  
76 sulfuric acid droplets. However, they did not model any other interactions between sulfuric acid  
77 and the sulfur particles beside coagulation. Krasnopolsky and Pollack (1994), meanwhile,  
78 showed that the lower cloud is formed by upwelling and subsequent condensation of sulfuric  
79 acid vapor due to the strong gradient in sulfuric acid mixing ratio below the clouds. James et al.  
80 (1997) showed that this process is very sensitive to the local eddy diffusion coefficient, and  
81 suggested that the variability of the lower and middle clouds was tied to the dynamical motions  
82 of the atmosphere in this region. This conclusion was also reached by McGouldrick and Toon  
83 (2007); they showed that organized downdrafts from convection and other dynamic processes  
84 could produce holes in the clouds. Indeed, observations from Pioneer Venus indicated that this  
85 region of the atmosphere has a lapse rate close to adiabatic, with parts of the middle cloud region  
86 being superadiabatic (Seiff et al. 1980; Schubert et al. 1980). Imamura and Hashimoto (2001)  
87 modeled the entire cloud deck, and reached many of the same conclusions as James et al. (1997)  
88 and Krasnopolsky and Pollack (1994) regarding the lower and middle clouds, and Toon et al.  
89 (1982) regarding the upper cloud. They also concluded that an upward wind may be necessary in  
90 order to reproduce the observations.

91         The clouds lie below an upper haze (UH), which extends from 70 to 90 km (Mills et al.  
92 2007). In Imamura and Hashimoto's model (2001), small cloud particles are lofted by upward

93 winds out of the top of the model domain, which would place them in this UH. This  
94 demonstrates that regional and/or global dynamical processes will lead to some mixing of the  
95 haze with the clouds, resulting in variability of the particle populations in the UH, especially if  
96 these processes vary with space and time. Though the variability of winds at the clouds-haze  
97 boundary has never been measured directly, we do observe the particle population variability. For  
98 instance, data from the Pioneer Venus Orbiter Cloud Photopolarimeter (OCPP) revealed  
99 latitudinal variations of an order of magnitude in haze optical thickness from the polar region  
100 (where it is more abundant) to the tropics, as well as temporal variations on the order of hundreds  
101 of days (Kawabata et al. 1980). More recently, Wilquet et al. (2009, 2012) used Venus Express  
102 SPICAV/SOIR solar occultation observations to show the existence of bimodality in the size  
103 distribution of the UH, with a small mode of radius 0.1-0.3  $\mu\text{m}$ , and a large mode of radius 0.4-  
104 1.0  $\mu\text{m}$ . These modes are not to be confused with the aforementioned modes 1, 2, and 3 in the  
105 cloud deck, even though they might be physically connected. Interestingly, the mean size of the  
106 haze particles as reported by Kawabata et al. from OCPP measurements 30 years earlier ( $0.23 \pm$   
107  $0.04 \mu\text{m}$ ) lies well within the small mode size range. In addition, Wilquet et al. (2009) find that  
108 the extinction of the haze was observed to vary by as much as an order of magnitude in a matter  
109 of days. The degree of variability also changed, as observations a few months later (Wilquet et  
110 al. 2012) showed variability in the magnitude of the haze extinction of only a factor of two. Time  
111 variability of the haze was also observed in infrared images of the Venus southern hemisphere,  
112 where the appearance of the haze changed dramatically across tens of degrees of latitude in the  
113 span of a few days (Markiewicz et al. 2007). The three studies above also showed that the haze  
114 optical depth can exceed unity, making it an active participant in the regulation of solar radiation  
115 reaching lower altitudes, and its variability a property that requires better understanding.

116 However, numerical models with adequate microphysics that include the UH are rare. Yamamoto  
117 and Tanaka (1998) and Yamamoto and Takahashi (2006) included the UH in their simulations of  
118 aerosol transport via global atmospheric dynamics and reproduced much of the observations  
119 satisfactorily. However, the aerosol microphysics in both studies is inadequate due to the lack of  
120 a detailed treatment of nucleation.

121 In this study, we investigate the formation and evolution of the UH and the cloud decks  
122 by constructing a one-dimensional (1D) microphysical and vertical transport model that couples  
123 the clouds to the haze with a more detailed treatment of the microphysics. We propose two  
124 possible causes for the bimodal size distribution and time variability of the haze: (1) the two  
125 modes are produced from two separate processes – one mode is derived from the *in situ*  
126 nucleation of sulfuric acid onto meteoric dust, a possibility discussed by Turco et al. (1983) for  
127 terrestrial atmospheres, and the other mode is made up of cloud particles that have been lofted  
128 into the UH via winds and eddy diffusion, and (2) the two modes and the time variability are  
129 entirely due to strong transient winds at the cloud tops lofting both mode 1 and mode 2 cloud  
130 particles into the UH.

131 We describe our basic model in section 2, with emphasis on the model attributes unique  
132 to our investigation of aerosols in the Venus atmosphere. In section 3 we present our model  
133 results, along with comparisons with data from Pioneer Venus and Venus Express. We also  
134 discuss our results in the context of physical processes involved in our model. We summarize our  
135 work and state our conclusions in section 4.

136

## 137 **2. MODEL**

138 We use version 3.0 of the Community Aerosol and Radiation Model for Atmospheres

139 (CARMA) as our base microphysical and vertical transport code. The model is an upgrade from  
140 the original CARMA (Turco et al. 1979, Toon et al. 1988) by Bardeen et al. (2008; 2011). We  
141 describe our model setup and departures from the base model below, and we refer the reader to  
142 Turco et al. (1979), Toon et al. (1988, 1989), and Jacobson et al. (1994) for detailed descriptions  
143 of the basic microphysics and vertical transport and English et al. (2011) for the sulfate  
144 microphysics in CARMA.

### 145 *2.1. Model Setup*

146 The microphysical and dynamical processes included in the model are the nucleation of  
147 liquid sulfuric acid droplets on sulfur and meteoric dust condensation nuclei; the condensational  
148 growth, evaporation, and coagulation of these particles; and their transport by sedimentation,  
149 advection and diffusion.

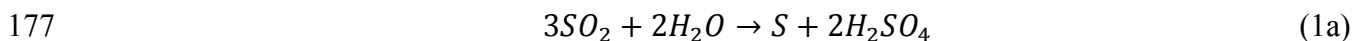
150 Table 1 summarizes the simulation parameters. The model atmosphere extends from 40 to  
151 100 km, covering the altitudes of the cloud deck and UH. This vertical range is split into 300  
152 levels of 200 m thickness each in our model. Our model time step is 10 seconds, and we found  
153 that a total simulation time on the order of  $2 \times 10^8$  seconds, or about 2000 Earth days, was  
154 necessary for the model to reach steady state. This is similar to the characteristic vertical  
155 diffusion time of the lower clouds as calculated from the eddy diffusion coefficient profile in  
156 section 2.4 and far greater than that of the Venus mesosphere (i.e. the altitudes of the upper cloud  
157 and upper haze) calculated by Imamura (1997).

158 In order to cover the size range from meteoric dust to large droplets and represent both  
159 volatile and involatile particles, we use two groups of particle bins, each covering the radius  
160 range from 1.3 nm to  $\sim 30 \mu\text{m}$ . The lower radius limit corresponds to the size of meteoric dust as  
161 described in Kalashnikova et al. (2000), while the upper radius limit mirrors the upper limit of

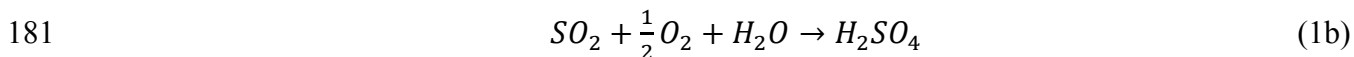
162 Imamura and Hashimoto's model (2001). The inclusion of multiple bins for involatile particles  
163 differs from the approach by Imamura and Hashimoto (2001), which only had the smallest  
164 particle size bin allocated to involatile particles.

165 Figure 1 shows the temperature and pressure profiles used (Seiff et al. 1985), which were  
166 fixed in the model. This is a simplification, as episodic increases in the temperatures of the Venus  
167 upper mesosphere and lower thermosphere have been known to exist since they were first  
168 observed by Clancy and Muhleman (1991). Such temperature increases have also been seen  
169 more recently by the Venus Express SPICAV and SOIR instruments (Bertaux et al. 2007) and the  
170 VeRa experiment (Tellmann et al. 2009). An increase in temperatures will suppress  $H_2SO_4$   
171 aerosol formation and enhance particle evaporation near the top of the domain studied here.  
172 These temperature fluctuations will have little direct impact on the particle populations at lower  
173 altitudes, but may indicate the presence of substantial changes in the dynamics of the  
174 mesosphere, which could affect particle transport.

175 The production rates of sulfur and sulfuric acid depend on the chemical pathways that  
176 lead to their production. Imamura and Hashimoto (2001) used



178 (Yung and DeMore 1982; Krasnopolsky and Parshev 1983) as their primary reaction. However,  
179 Yung and DeMore (1982) suggests that the main scheme for production of sulfuric acid is  
180 actually



182 where the sulfur produced during the reaction is converted to SO via reaction with  $O_2$ , though  
183 their model still shows a net production of S. Furthermore, equation 1a is derived from Yung and  
184 DeMore (1982)'s Model A, which is more appropriate for a Venus early in its evolution than the



185 current Venus. Meanwhile, Krasnopolsky and Parshev (1983) note that the reaction that would  
 186 normally generate S, SO + SO, could also go on to produce S<sub>2</sub>O instead. All of these  
 187 considerations suggest that the production rate of S is likely to be lower than half the production  
 188 rate of sulfuric acid, as suggested by equation 1a. On the other hand, Yung and DeMore (1982)  
 189 also showed that polysulfur can be produced and that sulfuric acid production (equation 1b) can  
 190 be suppressed via (SO)<sub>2</sub> dimer chemistry, while Toon et al. (1982) suggested that the primary  
 191 reaction can switch between equations 1a to 1b depending on the local O<sub>2</sub> content, which may be  
 192 variable. Therefore, it is uncertain what the sulfur production rate actually is. For simplicity, we  
 193 will use equation 1a as a basis for the production of sulfuric acid and sulfur, but we will also test  
 194 the effect of decreasing the sulfur production rate (section 3.3).

195 We begin each model run with no model-relevant species in the model box, e.g. no  
 196 sulfuric acid vapor or condensation nuclei of any kind. As each model run progresses, mass is  
 197 injected into the model atmosphere in the form of sulfuric acid vapor and involatile condensation  
 198 nuclei. The latter is split into two populations, one corresponding to photochemical products  
 199 (sulfur), and one corresponding to meteoric dust. Here, we assume a density of 1.9 g cm<sup>-3</sup> for the  
 200 condensation nuclei, as an average between the density of sulfur (1.8 g cm<sup>-3</sup>, Imamura and  
 201 Hashimoto 2001) and meteoric dust (2.0 g cm<sup>-3</sup>, Hunten et al. 1980). We use the same production  
 202 profiles of sulfuric acid vapor and photochemical condensation nuclei as Imamura and  
 203 Hashimoto (2001) for the production rates P<sub>H<sub>2</sub>SO<sub>4</sub></sub> and P<sub>CN</sub>, respectively:

$$204 \quad P_{H_2SO_4} = \Phi_p g(z) \text{ cm}^{-3} \text{ s}^{-1} \quad (2a)$$

$$205 \quad P_{CN} = \frac{1}{2} \Phi_p g(z) \left( \frac{\rho_{CN}}{M_s} \frac{4}{3} \pi r_{CN}^3 \right)^{-1} \text{ cm}^{-3} \text{ s}^{-1} \quad (2b)$$

206 where  $\Phi_p$  is the column-integrated production rate of sulfuric acid vapor; the function  $g(z)$  is a  
 207 Gaussian with a peak at 61 km altitude and full-width-half-max of 2 km such that

208 
$$\int_0^{\infty} g(z) dz = 1 \quad (2c)$$

209  $\rho_{\text{CN}}$  is the density of the condensation nuclei,  $1.9 \text{ g cm}^{-3}$ ;  $r_{\text{CN}}$  is the radius of the  
210 condensation nuclei; and  $M_s$  is the mass of a sulfur atom,  $5.34 \times 10^{-23} \text{ g}$ . Our results showed that  
211 agreement between model and data was best if  $\Phi_p$  was decreased from Imamura and  
212 Hashimoto's (2001) nominal value of  $10^{12} \text{ cm}^{-2} \text{ s}^{-1}$  to  $6 \times 10^{11} \text{ cm}^{-2} \text{ s}^{-1}$ , consistent with the  
213 suppression of the sulfuric acid production rate discussed in Yung and DeMore (1982). Our  
214 nominal production profiles are plotted in Figure 2.

215 The exact mechanics of how sulfuric acid nucleates onto condensation nuclei is not well  
216 understood and this is made worse by the complexities of the chemistry in the Venus atmosphere.  
217 As previously stated, we assume that the photochemical condensation nuclei are made of sulfur,  
218 similar to the strategy of Imamura and Hashimoto (2001). However, this is a simplification, as  
219 sulfur would likely exist in the form of polysulfur in the Venus clouds. Polysulfur would also  
220 undergo the processes of nucleation, condensation, and evaporation similar to sulfuric acid  
221 aerosols (Toon et al. 1982), with the only difference being that the polysulfur aerosols would  
222 likely be solid at the temperatures of the upper cloud (Lyons 2008; Zhang et al. 2012a) and  
223 therefore would not coagulate as efficiently as liquid aerosol droplets. Furthermore, as sulfuric  
224 acid cannot actually wet sulfur (Young 1983), polysulfur cannot act as condensation nuclei in the  
225 sense that they form cores that are completely encased within a layer of sulfuric acid. Instead, it  
226 is more likely that sulfuric acid will only condense on a fraction of the total surface of a  
227 polysulfur particle, and it is this small "drop" of condensed acid that then acts as the nucleation  
228 site for more sulfuric acid. Thus, the actual particles would be made up of a polysulfur particle  
229 stuck to the side of a droplet of sulfuric acid, with part of the polysulfur particle exposed to the  
230 atmosphere. As Young (1983) elucidates, this has the effect of decreasing the efficiency of

231 coagulation in the growth of these sulfuric acid aerosols, as now part of the surface is covered by  
232 polysulfur and will not be able to participate in coagulation. In addition, as coagulation occurs,  
233 more of the sulfuric acid particle's surface area will be covered by polysulfur (from particles it  
234 coagulated with), further decreasing its coagulation rate. This has the effect of eventually  
235 stopping coagulation altogether when the particle reaches a radius of  $\sim 10 \mu\text{m}$ . While our model  
236 does not distinguish whether the polysulfur "core" is within the sulfuric acid or attached to its  
237 side, it does assume, for coagulation, that the entire surface is "available". We will discuss the  
238 effect of this in section 3.1.

239 Further complicating the picture is the process opposite to the one we are modeling: the  
240 nucleation of polysulfur onto sulfuric acid particles (Young 1983; Lyons 2008). Whether one  
241 process dominates the other is determined by which particles homogeneously nucleates, i.e.  
242 which one appears "first" to act as the condensation nuclei for the other. In this case, as the  
243 saturation vapor pressure of most species of  $S_x$  is an order of magnitude or more lower than that  
244 of sulfuric acid in the cloud top region (Young 1983; Lyons 2008), we can safely assume that  
245 polysulfur will homogeneously nucleate before sulfuric acid does so as to act as its condensation  
246 nuclei and that we may ignore the opposite process. However, future studies should take into  
247 account the aerosol physics of the polysulfur nuclei to investigate its effects on the cloud  
248 distribution.

249 In our model, nucleation of sulfuric acid vapor onto the polysulfur condensation nuclei  
250 occurs when the ambient sulfuric acid vapor concentration reaches a critical supersaturation. This  
251 is determined by the sulfuric acid weight percent of the liquid that would form upon  
252 condensation (see section 2.2) and the curvature of the surface on which the vapor will condense.  
253 That is, we assume that the accommodation coefficient is unity. The curvature effect is

254 determined by the Kelvin equation (Seinfeld and Pandis 2006):

$$255 \quad \ln \frac{p}{p_o} = \frac{2\gamma M}{\rho r RT}. \quad (3)$$

256 For our case,  $p_o$  is the saturation vapor pressure over a flat surface;  $p$  is the saturation vapor  
257 pressure over a surface with curvature  $r$ ;  $\gamma$ ,  $M$ , and  $\rho$  are the surface tension, molar mass, and  
258 density of sulfuric acid, respectively;  $R$  is the gas constant; and  $T$  is the temperature. For  
259 reasonable values of these parameters corresponding to  $\sim 61$  km in the Venus atmosphere, where  
260 we use the parameterization of Mills (1996) for the surface tension, we find that the actual  
261 saturation vapor pressure over condensation nuclei becomes an order of magnitude greater than  
262 the saturation vapor pressure over a flat surface when the radius of the particle is  $\sim 2$  nm.  
263 However, given equation 2a, it will take on the order of hours for the sulfuric acid to build to  
264 such concentrations, during which time the polysulfur condensation nuclei will also be growing,  
265 thus increasing its radius of curvature and decreasing the saturation vapor pressure over its  
266 surface. Therefore, there may exist an equilibrium point where the sulfuric acid concentration is  
267 just high enough to begin nucleation onto the growing polysulfur particles. The calculation of  
268 this equilibrium point is beyond the scope of this work, however, as our knowledge of the  
269 kinetics of sulfur reactions is poor and thus we have ignored all microphysics (nucleation,  
270 condensation, coagulation) associated with the condensation nuclei. Therefore, we will make a  
271 simplification and assign a radius of  $\sim 10$  nm to the polysulfur condensation nuclei that are  
272 injected into the model. Toon et al. (1982) simulated the microphysics of sulfur particles, but did  
273 not take into account the effects of background sulfuric acid vapor or nucleation of said vapor on  
274 the sulfur particles. It would be ideal to combine these processes to create a more complete  
275 picture of the Venus clouds and hazes.

276 We adopt similar lower boundary conditions as those of Imamura and Hashimoto (2001),

277 where involatile (sulfur) particles of size  $\sim 0.17 \mu\text{m}$  (mode 1) are fixed to have a number density  
 278 of  $40 \text{ cm}^{-3}$  in accordance with LCPS data (Knollenberg and Hunten 1980). We set the mixing  
 279 ratio of  $\text{H}_2\text{SO}_4$  to be 3 ppm at the lower boundary, within the 0-4 ppm estimates from analysis of  
 280 Magellan radio occultation observations by Kolodner and Steffes (1998). We adopt a zero flux  
 281 boundary condition for the top boundary, as we assume that no particles or  $\text{H}_2\text{SO}_4$  vapor escape  
 282 the mesosphere above 100 km.

## 283 2.2. Thermodynamics of $\text{H}_2\text{SO}_4$

284 Of particular importance in this model is the treatment of certain thermodynamic  
 285 properties of  $\text{H}_2\text{SO}_4$ , such as its saturation vapor pressure and surface tension. Both of these  
 286 quantities control whether a sulfuric acid droplet is growing by condensation or evaporating.

287 The saturation vapor pressure  $p_{\text{H}_2\text{SO}_4}$ , in units of atm, is calculated via the equation of  
 288 Ayers et al. (1980), modified by Kulmala and Laaksonen (1990):

$$289 \quad \ln p_{\text{H}_2\text{SO}_4} = \ln p_{\text{H}_2\text{SO}_4}^0 + 10156 \left[ -\frac{1}{T} + \frac{1}{T_0} + \frac{0.38}{T_c - T_0} \left( 1 + \ln \frac{T_0}{T} - \frac{T_0}{T} \right) \right] - \frac{H}{RT} \quad (4a)$$

290 where  $T$  is temperature,  $R$  is the universal gas constant,  $T_0 = 340 \text{ K}$  is a reference temperature,  $T_c$   
 291  $= 905 \text{ K}$  is the critical temperature,  $p_{\text{H}_2\text{SO}_4}^0$  is a reference pressure given by:

$$292 \quad \ln p_{\text{H}_2\text{SO}_4}^0 = -\frac{10156}{T_0} + 16.259 \quad (4b)$$

293 and  $H$  is the enthalpy associated with the mixing of water and sulfuric acid, given by the  
 294 parameterization of Giaque (1959):

$$295 \quad H = 4.184 \times 10^7 \left[ 23624.8 - \frac{1.14208 \times 10^8}{4798.69 + (W_{\text{H}_2\text{SO}_4} - 105.315)^2} \right] \text{ erg mol}^{-1} \quad (4c)$$

296 where  $W_{\text{H}_2\text{SO}_4}$  is the weight percentage of  $\text{H}_2\text{SO}_4$  in the aerosol droplet calculated from  
 297 Tabazadeh et al. (1997) as a parameterization to temperature and background water vapor  
 298 concentration.

299 The surface tension is derived from data collected by Sabinina and Turpugow (1935)  
300 parameterized linearly with respect to temperature by Mills (1996). The value of the surface  
301 tension at ~61 km is given in Table 1.

### 302 2.3. Water Vapor Profile

303 The base CARMA model does not treat the exchange of water between the background  
304 water vapor concentration and the water taken up in the sulfuric acid cloud particles as they  
305 grow. Instead, the weight percentage of water and sulfuric acid is always such that there is  
306 equilibrium between the particle and the background water vapor concentration. In other words,  
307 the model assumes the equilibrium aerosol growth regime (Zhang et al. 2012b). However, this  
308 may not necessary be true given the low water vapor concentration in the Venus atmosphere  
309 (Ignatiev et al. 1997). Therefore, we will assume an equilibrium background water vapor profile  
310 that is fixed in time. Figure 3 shows this profile. Above 60 km, we assume a water vapor  
311 concentration of ~1 ppm in accordance with observations by Bertaux et al. (2007). Below 60 km,  
312 we model our profile after Model A of Ignatiev et al. (1997) and data from Venera 11, 13, and 14  
313 (also taken from Ignatiev et al. 1997). The profile is empirically determined using an arctangent  
314 function to connect the region above 60 km to the region below, and a Gaussian function to take  
315 into account the water vapor concentration maximum at ~53 km in Model A of Ignatiev et al.  
316 (1997). The formula for the water vapor concentration (partial pressure),  $P_{\text{H}_2\text{O}}$ , is then

$$317 \quad P_{\text{H}_2\text{O}} = 6 \times \exp \left[ - \left( \frac{z-53}{8} \right)^2 \right] - 14.5 \left( \frac{z}{\pi} \right) \tan^{-1}(0.5z - 32.5) + 15.5 \text{ ppm} \quad (5)$$

318 where  $z$  is in kilometers.

### 319 2.4 Eddy Diffusion

320 The eddy diffusion coefficient profile is shown in Figure 4. The values between 40 and  
321 70 km altitude are approximated from Imamura and Hashimoto (2001) by fitting a function

322 consisting of the sum of an exponential and a Gaussian function. The large increase in eddy  
 323 diffusion coefficient at  $\sim 53$  km simulates the convective overturning present in the middle cloud  
 324 as inferred from Schubert et al. (1980) and measured *in situ* by the VEGA Balloons (Ingersoll et  
 325 al. 1987; Crisp et al. 1990). The eddy diffusion coefficient above 70 km is approximated as a  
 326 Gaussian from Fig. 11 of Krasnopolsky (1983), which itself is generated from continuity  
 327 arguments with respect to the aerosol distribution observed in this region at the time. The  
 328 empirical formula of the eddy diffusion coefficient,  $K_{zz}$ , as a function of altitude  $z$  in kilometers  
 329 above 40 km is then:

$$330 \quad K_{zz} = 10^{\frac{4z-160}{38.55}} + 2500000 \left\{ \exp \left[ - \left( \frac{z-52.5}{1.201} \right)^2 \right] + \exp \left[ - \left( \frac{z-100}{12.01} \right)^2 \right] \right\} \text{ cm}^2 \text{ s}^{-1} \quad (6)$$

331 To implement eddy diffusion in CARMA 3.0, we adopt similar numerical methods used by the  
 332 model to implement Brownian diffusion, except we replace the density of the species by its  
 333 mixing ratio. The upward and downward velocities of eddy diffusion of species  $j$ ,  $v_u^j$  and  $v_d^j$ ,  
 334 respectively, are then given by:

$$335 \quad v_u^j = \ln \left( \frac{f_i^j}{f_{i-1}^j} \right) \frac{K_{zz}}{dz} \frac{f_{i-1}^j}{f_i^j - f_{i-1}^j} \text{ cm s}^{-1} \quad (7a)$$

$$336 \quad v_d^j = \ln \left( \frac{f_i^j}{f_{i-1}^j} \right) \frac{K_{zz}}{dz} \frac{f_i^j}{f_i^j - f_{i-1}^j} \text{ cm s}^{-1} \quad (7b)$$

337 where  $dz$  is the thickness of an atmospheric layer (200 m in our model) and  $f_i^j$  is the mixing ratio  
 338 of species  $j$  in the  $i$ th layer. We can see that equations 7a and 7b are diffusion velocities by  
 339 considering the continuous limit, where  $\text{Ln}(f_i/f_{i-1}) = \text{Ln}(f_i) - \text{Ln}(f_{i-1}) \sim d\text{Ln}f = df/f$ , and  $f_i - f_{i-1} =$   
 340  $df$ ; the two  $df$ 's and  $f$ 's then cancel, resulting in  $K_{zz}/dz$ , which is an eddy diffusion velocity scale.  
 341 This velocity is modulated by the mixing ratio gradient in our discrete case (i.e.  $\text{Ln}(f_i/f_{i-1})$  does  
 342 not cancel with  $f_i/(f_i - f_{i-1})$ ) such that large gradients lead to large velocities. The natural log  
 343 prevents numerical instabilities in the event the denominator becomes too small.

344 2.5. *Meteoric Dust*

345 Turco et al. (1983) discussed the properties of meteoric dust in the Venus atmosphere and  
346 concluded that it is similar to meteoric dust in the atmosphere of Earth and could act as  
347 condensation nuclei to water vapor, forming thin ice hazes. We propose that meteoric dust could  
348 also serve as condensation nuclei to sulfuric acid vapor, as its saturation vapor pressure is  
349 extremely low at the altitude of the UH, on the order of  $10^{-19}$  mbars for pure sulfuric acid, and  
350  $10^{-31}$  mbars for a water-sulfuric acid mixture with 75 wt% sulfuric acid (Kulmala and Laaksonen  
351 1990) that is typical of the UH (Kawabata et al. 1980). Thus, any sulfuric acid vapor that is lofted  
352 into the UH by diffusion or winds could potentially condense on the meteoric dust present in this  
353 region.

354 The Kelvin effect may play a large role in limiting the efficiency of meteoric dust as  
355 condensation nuclei due to their small size. However, if we use the appropriate values for  
356 sulfuric acid in the UH and a typical condensation nuclei size of 1.3 nm (Kalashnikova et al.  
357 2000), then equation 3 yields an approximate increase of 2.4 orders of magnitude in the  
358 saturation vapor pressure. This gives a resulting saturation vapor pressure of  $\sim 10^{-29}$  -  $10^{-28}$   
359 mbars, which is far less than recent upper limits on the abundance of  $\text{H}_2\text{SO}_4$  in the UH, e.g. 3  
360 ppb, or about  $3 \times 10^{-9}$  mbar at 80 km, from Sandor et al. (2012). Therefore, meteoric dust should  
361 act as very efficient condensation nuclei as long as the actual  $\text{H}_2\text{SO}_4$  mixing ratio is not  
362 significantly lower than this upper limit, even if the Kelvin effect is considered.

363 Meteoric dust is treated in the same way in our model as the sulfur condensation nuclei.  
364 However, it is clear that meteoric dust, which is typically made of silicates (Hunten et al. 1980),  
365 may react differently to sulfuric acid than sulfur. For example, Saunders et al. (2012) showed that  
366 silicates dissolve in sulfuric acid on a timescale of an Earth week at the temperatures of the cloud



367 tops. However, once the sulfuric acid droplet becomes much larger than the nucleus it condensed  
368 on, the dissolution of said nucleus should have very little effect on the rest of the particle.

369 The production profile of meteoric dust we use in our model is shown in Figure 5 as an  
370 empirical approximation of the profile calculated by Kalashnikova et al. (2000). All meteoric  
371 dust particles are assumed to have a radius of 1.3 nm. We have shifted the profile maximum from  
372 87 km to 83 km in order to match the maximum in the small mode curve in Fig. 9 of Wilquet et  
373 al. (2009). The parameterization of the profile is given by:

$$374 \quad P_{md} = \begin{cases} 5 \times 10^{-3} e^{-\left(\frac{z-83}{2.402}\right)^2} & z \leq 83 \\ 5 \times 10^{-3} e^{-\left(\frac{z-83}{8.407}\right)^2} & z \geq 83 \end{cases} \quad (8)$$

375 where  $z$  has units of kilometers and  $P_{md}$  has units of  $\text{cm}^{-3} \text{s}^{-1}$ . Though this profile was applied to  
376 Earth only, we will assume that it is also applicable to Venus due to the two planets' similarities.  
377 However, if atmospheric density is the determining factor of the altitude of peak meteoric dust  
378 ablation (e.g. Gadsden 1968) then our profile may be too low in the atmosphere. This is due to  
379 the fact that the altitude on Venus with the same atmospheric density as that of the peak ablation  
380 altitude on Earth is actually  $\sim 110$  km.

## 381 2.6. Winds

382 In addition to testing the effects of the nucleation of sulfuric acid droplets on meteoric  
383 dust on the UH particle size distribution, we will also test the effects of transient gusts at the  
384 cloud tops. These are a separate set of simulations from the nominal runs described in section  
385 2.1, though they do use the results of the nominal runs as initial conditions. Figure 6 shows the  
386 wind profile we use to test the effects of transient upward winds on the number density and size  
387 distribution of the cloud and haze aerosols. The wind beneath 70 km is a constant flux wind  
388 similar to that of Imamura and Hashimoto (2001) but increased in strength by two orders of

389 magnitude to simulate a gust as opposed to a branch of the global circulation:

$$390 \quad w = \frac{8.0 \times 10^{-3}}{\rho} \text{ cm s}^{-1} \quad (9)$$

391 where  $w$  is upward wind speed and  $\rho$  is atmospheric density, both in cgs units. In order to adhere  
392 to our top boundary condition and simulate turning over of the wind currents, we allow the  
393 upward wind to fall off linearly above 70 km so that it vanishes at 75 km. This is consistent with  
394 the strong static stability above that altitude.

395         Recent Venus Express observations of the Venus southern polar vortex at the altitude of  
396 the upper cloud (63 – 69 km) show divergent and convergent circulations that imply vertical  
397 velocities of  $\sim 0.2 \text{ m s}^{-1}$  (Garate-Lopez et al. 2013), roughly consistent with the lower limits of  
398 our upper cloud wind velocities, though most of the vertical motions were downward rather than  
399 upward. In addition, convective cells at the cloud tops have been observed at and downwind of  
400 the Venus subsolar point (Belton et al. 1976; Titov et al. 2012). These have been interpreted  
401 using 2D convection simulations as the incursion of the convective region in the middle cloud  
402 into the stably stratified upper cloud (Baker et al. 1998; 1999), though some recent observations  
403 suggest that the convective layer is thin enough that it may only occupy the upper cloud itself  
404 (Markiewicz et al. 2007). The results of Baker et al. (1998) suggest that gravity waves  
405 originating from the enlarged convective region could produce vertical velocities of  $1\text{-}2 \text{ m s}^{-1}$  at  
406 and above 60 km, matching our wind velocities at those altitudes.

407         Nevertheless, there are clear differences between our vertical advection scheme and the  
408 actual advection processes in the Venus clouds. For instance, a realistic treatment of the gust  
409 “turning over” above 70 km requires horizontal transport, which is beyond the scope of this  
410 study. Thus, for the purpose of this work we will only examine qualitatively the effects of such a  
411 gust on the cloud profile, such as the formation of a detached haze due to upwelled cloud

412 particles, its destruction due to sedimentation and diffusion, the time scales involved, and the  
413 changes in particle size distributions. In order to better evaluate these effects, we will magnify  
414 them by considering gusts that last for  $5 \times 10^4$  seconds, or  $\sim 14$  Earth hours. Gusts in the polar  
415 vortex may last as long, though as Venus Express orbits Venus on the same time scale ( $\sim 1$  Earth  
416 day), the actual duration is uncertain. Winds caused by subsolar point convection may also be  
417 able to last 14 hours, as convective features were seen up to  $50^\circ$  latitude away from the equator  
418 (Titov et al. 2012). This should also apply to longitude, and a distance of  $50^\circ$  longitude away  
419 from the subsolar point can be covered by the  $\sim 100 \text{ m s}^{-1}$  planet-encircling zonal winds at the  
420 cloud tops (Schubert et al. 1980) in about 14 hours. In other words, each parcel of air could have  
421 14 hours during which gusts arising from subsolar convection can disrupt the aerosol particle  
422 distributions therein before the convective cells give way to stably stratified regions.  
423 Nevertheless, not only is the wind unlikely to be constant given the turbulent nature of its origin,  
424 but Wilquet et al. (2009) observed the haze at  $\sim 70^\circ \text{ N}$ , a full  $20^\circ$  latitude away from the  
425 convective region. In short, we are not looking for exact agreement between our particle number  
426 density and size distributions and one that is retrieved from observations, but rather whether we  
427 can qualitatively reproduce the chaotic behavior of the UH.

428

### 429 **3. RESULTS AND DISCUSSION**

430 Our steady state results do not show a stable equilibrium distribution, but rather a quasi-  
431 periodically varying distribution. Thus, we will proceed to compare to observations our results  
432 from a single time step near the end of our nominal model run that best match them (section 3.1),  
433 and then describe the mechanisms that could allow for such dynamics to occur despite a constant  
434 background atmospheric state (section 3.2). In section 3.3 we discuss the effect of decreasing the

435 sulfur production rate, and in section 3.4 we will describe our transient wind results.

### 436 *3.1 Nominal Results*

437 Figure 7 shows the number density predictions from our model for particles with radii  
438 greater than  $\sim 0.1 \mu\text{m}$ , which we choose as the lower size boundary of mode 1/small mode  
439 particles (Wilquet et al. 2009). We see that it is largely consistent with LCPS cloud data  
440 (Knollenberg and Hunten 1980), though the middle cloud is overestimated by a factor of 3 and  
441 the lower cloud is underestimated by a factor of  $< 2$ . These differences are well within the range  
442 of variability seen at these levels by the Pioneer Venus entry probes (Esposito et al. 1983), or in  
443 near infrared observations of the Venus night side (Crisp et al. 1990; Grinspoon et al. 1993).  
444 Figure 8 shows the size distributions of the cloud and haze particles at various altitudes. It  
445 reproduces both the high number density of mode 1 particles in the upper cloud and the distinct  
446 multi-modal nature of the middle and lower clouds' particle size distributions as seen by Pioneer  
447 Venus (Knollenberg and Hunten 1980), including mode 1 at  $\sim 0.2 \mu\text{m}$ , mode 2 at  $\sim 1.4 \mu\text{m}$ , and  
448 mode 3 (near the cloud base) at  $\sim 3.5 \mu\text{m}$ . Comparison of this size distribution with Pioneer Venus  
449 observations at 54.2 km (Knollenberg and Hunten 1980) shows clear agreement between the  
450 model mode radii and that of the data, though a discrepancy exists in the mode abundances –  
451 there is an order of magnitude less mode 3 particles and  $\sim 3$  times more mode 2 particles in our  
452 model than in the observations. These discrepancies could be caused by the lack of transient  
453 gusts in the middle and lower clouds of our steady state model, which Imamura and Hashimoto  
454 (2001) showed could be used to produce a multi-modal structure in their model. Physically,  
455 vertical gusts such as those detected in the middle cloud by the VEGA Balloons (Crisp et al.  
456 1990) would both aid in the growth of mode 2 particles into mode 3 particles by introducing  
457 “fresh” sulfuric acid from below (updrafts) and in the depletion of the middle cloud by

458 downwelling the cloud particles (downdrafts); the depletion of the middle cloud is also a natural  
459 consequence of the growth of particles, as these larger particles would have a faster  
460 sedimentation time. Therefore, a series of vertical updrafts and downdrafts could lead to fewer  
461 mode 2 particles, more mode 3 particles, and fewer particles in the middle cloud, resulting in  
462 better agreement with data.

463         We assume that mode 3 particles are just larger versions of mode 2 particles, i.e. they are  
464 liquid sulfuric acid droplets with a solid polysulfur component, but this need not be the case. In  
465 fact, Knollenberg and Hunten (1980) discussed the possibility that mode 3 is made up of solid,  
466 crystalline particles. On the other hand, Toon et al. (1984) suggested that mode 3 is in fact a large  
467 particle tail of mode 2; our results support this latter interpretation, as the mode 3 particle peak  
468 blends into the mode 2 peak somewhere between 54 and 58 km (figure 8). In light of the results  
469 of Young (1983), however, we must consider the effect of solid polysulfur “patches” on the  
470 surface of our sulfuric acid particles, which may make them seem like solid, crystalline particles  
471 if the polysulfur coverage is high enough. As previously stated, the effect of these patches is the  
472 decrease in the efficiency of coagulation in the removal of smaller particles, creating a smaller  
473 number of larger particles. This could explain our underestimation of the lower cloud particle  
474 number density, though it would also further overestimate our middle cloud particle number  
475 density. Thus, a combination of decreased coagulation efficiency in larger particles and the  
476 addition of middle cloud vertical gusts may be necessary to improve our model’s agreement with  
477 the Pioneer Venus Sounder Probe observations.

478         In the UH, our model predicts a steady state size distribution that is roughly mono-modal,  
479 with a small “bump” at radii  $> 1 \mu\text{m}$  corresponding to upwelled mode 2 particles that is largely  
480 insignificant compared to the rest of the distribution. The lack of distinct bimodality despite the

481 two different sources of particles is likely due to the effects of coagulation. In Figure 9, we  
 482 follow the time evolution of the upper haze at an altitude of 84 km during the first ~4 months of  
 483 the model run, long before steady state is reached. The green “bar” at 0.01  $\mu\text{m}$  is caused by the  
 484 artificial injection of 10 nm photochemical condensation nuclei into the model domain and  
 485 should be ignored. Immediately after the start of the simulation, a haze population emerges with  
 486 particle radii  $< 10$  nm. Such small particles could have only resulted from the nucleation of  
 487 sulfuric acid onto meteoric dust and subsequent condensational growth. Cloud droplets reach 84  
 488 km one week later due to upward diffusion, which is followed by the disappearance of the  
 489 original meteoric-dust-derived haze population about a month afterwards. This suggests a  
 490 coagulation timescale of about a month to decrease the original population by about 2-3 orders of  
 491 magnitude, if indeed coagulation is the cause of this result. We can test whether this is physically  
 492 viable using the simplified solution to the discrete coagulation equation  $N(t)$ :

$$493 \quad N(t) = \frac{N_0}{1+(t/\tau_c)} \quad (10a)$$

494 where

$$495 \quad \tau_c = \frac{2}{KN_0} \quad (10b)$$

496 is a coagulation timescale. Here,  $N_0$  is the original number density, and  $K$  is the coagulation  
 497 kernel. For simplicity we use the continuum regime kernel, as particle number density is small,  
 498 and assume that the particle radii  $R_2 \gg R_1$ :

$$499 \quad K \sim \frac{2kT R_2}{3\mu R_1} \quad (11)$$

500 (Seinfeld and Pandis 2006). For a Boltzmann’s constant  $k = 1.38 \times 10^{-16}$  erg  $\text{K}^{-1}$ , temperature  $T \sim$   
 501 160 K, atmospheric viscosity  $\mu \sim 8 \times 10^{-5}$  g  $\text{cm}^{-1}$   $\text{s}^{-1}$  and particle radii  $R_1 = 1$  nm and  $R_2 = 100$   
 502 nm, we get a coagulation time needed to reduce the number density by ~2-3 orders of magnitude  
 503 of a few months, similar to our model results. Therefore we can conclude that the UH is likely a

504 combination of upwelled cloud particles and particles nucleated *in situ* on meteoric dust, but that  
505 the latter population has “fused” with the former, resulting in a mono-modal size distribution in  
506 steady state. Thus, two separate sources of particles – one upwelled from below, and one  
507 nucleated *in situ* cannot explain the bimodality detected by Kawabata et al. (1980) and Wilquet et  
508 al. (2009). However, our peak model cloud top haze particle radius,  $\sim 0.3 \mu\text{m}$  at 70 km, is fairly  
509 close to the average haze particle radius originally detected by Kawabata et al. (1980) ( $0.23 \pm$   
510  $0.04 \mu\text{m}$ ). Furthermore, our UH size distribution covers the size range of both the small and the  
511 large mode detected by Wilquet et al. (2009). Therefore, we propose that our results represent  
512 both modes, and that something else is responsible for the splitting of the particle population into  
513 two distinct modes. Figure 7 shows a comparison between the model number density and the  
514 sum of the number densities of the two modes detected by Wilquet et al. (2009). The agreement  
515 between model and data is satisfactory up to 80 km, above which the model underestimates the  
516 number density by about half an order of magnitude.

517         Alternatively, the meteoric dust production profile could be at a much higher altitude (see  
518 section 2.5) such that they are above the upwelled cloud particles; the sulfuric acid droplets that  
519 nucleate onto these meteoric dust particles would then have time to grow before they sediment  
520 into the altitudes dominated by cloud droplets, with which they will coagulate as before. In this  
521 scenario, the small mode would consist of both the upwelled cloud particles and the sedimenting  
522 particles that nucleated *in situ* onto meteoric dust, while the larger mode would be made up of  
523 the products of small mode coagulation. However, the resulting smaller  $R_2/R_1$  ratio (equation 11)  
524 would increase the coagulation time scale and decrease the amount of large mode particles that  
525 can be produced. Ultimately, the particles that nucleate from meteoric dust may be  
526 inconsequential due to the lower flux of meteoric dust as compared to the flux of sulfuric acid

527 vapor and sulfur.

528           Figure 10 shows a comparison between the predicted mixing ratio of sulfuric acid vapor  
529 and the observed mixing ratio from Magellan radio occultation data as analyzed by Kolodner and  
530 Steffes (1998). Though the large dispersion in the data from 0-6 ppm allows for a wide variety of  
531 results to “fit” it, the physically relevant results are likely those that exhibit a local sulfuric acid  
532 maximum below the clouds, and which also fit the nonzero data points. Indeed, our model results  
533 show a satisfactory fit to the data points. While the bottom boundary condition fixes the vapor  
534 concentration to 3 ppm at 40 km, the vapor concentration peak of ~4.5 ppm at the cloud base is  
535 entirely due to sedimenting particles evaporating and depositing their sulfuric acid vapor at that  
536 altitude. The peak value reflects a balance between the rate of vapor deposition and the upward  
537 and downward vapor diffusion, and also imposes a constraint on the altitude of the cloud base,  
538 below which any sulfuric acid droplets will be evaporating. Our results show that the cloud base  
539 is at ~47 km, consistent with the model results of Krasnopolsky and Pollack (1994). Above the  
540 cloud base, the vapor profile largely follows the saturation vapor pressure curve except at (1) 61  
541 km, where sulfuric acid vapor is photochemically produced, and (2) above 80 km. This latter  
542 deviation may be caused by numerical instabilities caused by the low saturation vapor pressure  
543 ( $\sim 10^{-31}$  mbars) or the phase properties of sulfuric acid and water solutions in this region  
544 (McGouldrick et al. 2011).

545           Figure 11 shows number density as a function of both altitude and particle radius, while  
546 figure 12 shows the sulfuric acid and particle mass fluxes for the middle cloud (top) and the  
547 other altitudes (bottom); together they give a summary of the processes occurring in the clouds  
548 and UH of Venus. The production of involatile sulfur condensation nuclei causes the nucleation  
549 and condensational growth of liquid sulfuric acid droplets at 61 km, resulting in a high number



550 density of mode 1 particles. These particles then diffuse upwards and sediment downwards. The  
551 positive divergence in the particle flux (in units of mass equivalent to  $10^{12}$  sulfuric acid  
552 molecules per unit area per second, where each molecule has mass  $\sim 1.6 \times 10^{-22}$  g) in this region  
553 is clearly shown by the positive slope at  $\sim 61$  km in the lower panel of Figure 12 – particles  
554 higher up has a smaller downward flux (i.e. a less negative flux) than the particles lower down.  
555 There is no corresponding slope in the vapor flux curve as all the vapor is condensing onto the  
556 particles. In the UH, the upward diffusion of particles appears to balance the sedimentation,  
557 leading to a near zero particle flux; the sulfuric acid vapor flux is also very close to zero, but it is  
558 likely due to the small amount of vapor at these altitudes.

559 Below 61 km, the vigorous convection in the middle cloud drives the large upward flux  
560 of sulfuric acid vapor (top panel of figure 12), resulting in enhanced production of mode 2  
561 particles as well as a tail of even larger particles resulting from coagulation. These particles, like  
562 the upper cloud particles, are transported downwards by sedimentation and upwards by diffusion.  
563 The latter process leads to a small large particle bump in the UH. These particles evaporate upon  
564 reaching the cloud base, leading to the regeneration of mode 1 particles and the deposition of  
565 sulfuric acid vapor beneath the clouds. The regenerated mode 1 is larger than the mode 1 of the  
566 upper cloud due to the coagulation of the droplets higher up in the clouds – the cores of these  
567 droplets are in effect added together, leading to the generation of larger involatile particles as the  
568 larger cores are exposed upon droplet evaporation. This may not be what actually happens if the  
569 “cores” are instead patches of polysulfur decorating the outside of the sulfuric acid droplets, as  
570 per the “gumdrop” model of Young (1983). In this case, the “cores” would not be added together  
571 and would remain the same size as their upper cloud counterparts upon the evaporation of the  
572 sulfuric acid. Meanwhile, the tail of large particles forms a distinct third mode upon evaporation

573 due to its slower evaporation rate as compared to that of the smaller mode 2 particles, which is a  
574 product of the Kelvin effect (equation 3).

575 Below the clouds, the sulfuric acid vapor exhibits a negative flux as discussed previously,  
576 while the particle flux is similarly negative, as the particles are sedimenting out of the bottom of  
577 the model domain. The absolute value of the sum of the two fluxes at the bottom of the model  
578 domain is  $\sim 9 \times 10^{11} \text{ cm}^{-2} \text{ s}^{-1}$ , slightly higher than the sum of the input flux of meteoric dust ( $\sim 5 \times$   
579  $10^5 \text{ cm}^{-2} \text{ s}^{-1}$ ), photochemical condensation nuclei ( $\sim 10^{11} \text{ cm}^{-2} \text{ s}^{-1}$ ), and sulfuric acid vapor ( $6 \times$   
580  $10^{11} \text{ cm}^{-2} \text{ s}^{-1}$ ). This is due to the quasi-periodically varying nature of our results, i.e. we have  
581 examined our simulated Venus cloud-haze system at a time when the flux out of the lower model  
582 boundary is higher than what it should be for a steady state ( $\sim 6.835 \times 10^{11} \text{ cm}^{-2} \text{ s}^{-1}$ ).

### 583 *3.2. Periodic Behavior and Precipitation on Venus*

584 Figure 13 shows the time evolution of the particle size distribution at various altitudes.  
585 Above the clouds, the quasi-periodic variations are very small, with amplitudes of no more than  
586 10%. In the upper cloud, the variations are larger with small hints of quasi-periodicity in the  
587 mode 2 particle abundances apparent, but the size distribution is dominated by mode 1 particles,  
588 which are fairly stable. In contrast, the middle cloud shows variations in particle abundances of  
589 several orders of magnitude. All three modes appear to grow in radii with time and are  
590 subsequently replaced with smaller particles on a time scale of  $\sim 6$  Earth months. In particular,  
591 mode 1 slowly grows to larger radii via coagulation and condensation until reaching  $\sim 0.25 \mu\text{m}$ ,  
592 where there is a rapid growth of particles to mode 2. This actually occurs at several points during  
593 the slow migration of mode 1 particles to larger radii, as the intense eddy diffusion at 54 km will  
594 allow any particles large enough to overcome the Kelvin barrier to grow rapidly. The upward  
595 diffusion of mode 1 particles from below then “resets” the mean mode 1 particle radius back to

596 ~0.2  $\mu\text{m}$ . Mode 2 then also grow slowly with time before growing somewhat rapidly into mode 3  
597 particles, which then proceed to sediment into lower altitudes. The increase in mode 2 particle  
598 growth rate occurs at nearly the same time as the rapid growth of mode 1 particles into mode 2  
599 particles, possibly due to the coagulation of the “new” mode 2 particles among themselves and  
600 with the “old” mode 2 particles, leading to the creation of the larger mode 3 particles.

601 Figure 13 also shows that, in comparison with the nominal/best-fit results in section 3.1,  
602 the “usual state” of the Venus clouds is actually not those observed by the LCPS – for the  
603 majority of the time, mode 2 has a mean radius of  $\sim 1.2 \mu\text{m}$  instead of the observed  $1.4 \mu\text{m}$   
604 (Knollenberg and Hunten 1980), and it only grows to such a size right before the emergence of a  
605 “new” mode 2.

606 This oscillation is apparently perpetuated by the growth of mode 1 particles into sizes  
607 capable of overcoming the Kelvin Barrier, as that leads to the perturbation of the established  
608 mode 2 particles which in turn leads to their growth into mode 3 particles. The growth of mode 1  
609 particles can occur via coagulation among themselves, though it is more likely that the majority  
610 of coagulation events are with the large number of smaller particles we use in our model as  
611 photochemical condensation nuclei and which grew from those nuclei but have not yet reached  
612 the sizes of the mode 1 particles, as coagulation between particles of vastly difference sizes is  
613 faster than coagulation between similarly sized particles (Seinfeld and Pandis 2006). As such,  
614 since each coagulation event would only add a very small amount of mass to each mode 1  
615 particle, the growth would be gradual but steady, matching what we see in our model results. It is  
616 interesting to note that this does not happen when we use a larger particle as our photochemical  
617 condensation nuclei (e.g. Imamura and Hashimoto (2001)), as coagulation would be much  
618 slower and “random” in time. These variations also do not happen to such an extent in the UH, as

619 both the coagulation kernel (equation 11) and condensational growth rate are much lower there.

620         The quasi-periodic variability of the middle cloud leads to a quasi-periodic sedimentation  
621 flux for the largest particles, which leads to the larger-than-expected bottom boundary flux in  
622 figure 11. Figure 14 shows the time evolution of the sulfuric acid vapor and particle flux out of  
623 the bottom boundary of the model domain, expressed in the same units as figure 12. The average  
624 of these oscillations,  $6.765 \times 10^{11} \text{ cm}^{-2} \text{ s}^{-1}$  matches the injection rate of mass into the model  
625 domain,  $6.835 \times 10^{11} \text{ cm}^{-2} \text{ s}^{-1}$  fairly well, indicating that we are indeed at an equilibrium state.  
626 Finally, we note that the particle and vapor flux oscillations are in phase with each other, and that  
627 the latter has greater amplitude than the former. This is explained by the evaporation of the  
628 particles below the cloud deck at  $\sim 47$  km, such that the sulfuric acid variations from the middle  
629 cloud are mostly expressed in the resulting vapor.

630         The possibility of such long term, quasi-periodic particle size variations provide  
631 tantalizing hints towards possible sulfuric acid “rain” below the cloud decks of Venus, though we  
632 use the term loosely as the downward mass fluxes associated with the “rain” in our model results  
633 are far smaller than that of typical rain events on Earth. Nonetheless, it would be interesting to  
634 search for evidence of their existence in VIRTIS observations of the Venus night side, which are  
635 sensitive to such variations in particle population.

### 636 *3.3 Variations in the Sulfur Production Rate*

637         As discussed in section 2.1, the production rate of sulfur in the Venus atmosphere may be  
638 much lower than half the production rate of sulfuric acid as implied by equation 1a due to  
639 reactions of S with  $\text{O}_2$  and the formation of  $\text{S}_2\text{O}$  instead of  $\text{SO}_2$  and S from the reaction  $\text{SO} + \text{SO}$ .  
640 To address the effect decreasing the sulfur production would have on our results we rerun our  
641 model with both one order of magnitude less sulfur produced and two orders of magnitude less

642 sulfur produced. Figure 15 shows our results in terms of the number density (top) and size  
643 distribution at 54 km in the middle cloud (bottom). Decreasing the sulfur condensation nuclei  
644 production rate decreases the number of cloud droplets produced at all altitudes, but also  
645 increases the average size of the droplets, since there are fewer nuclei for the same amount of gas  
646 to condense on. Mode 1 particle abundances also decrease significantly in the middle cloud when  
647 sulfur production is reduced, as the relative fraction of mode 1 particles that grow to mode 2  
648 particles is now much larger. The disagreement between the observed size distribution and the  
649 results of the reduced sulfur cases suggest that either (1) the primary reaction in the production of  
650 sulfur is indeed reaction 1a (section 2.1), and that  $O_2$  is relatively scarce in the upper cloud, or  
651 (2) Pioneer Venus took data during a period of time when  $SO_2$  abundance exceeded  $O_2$   
652 abundance, perhaps due to an updraft (Toon et al. 1982), and that the “steady state” size  
653 distribution in the middle cloud is more akin to the reduced sulfur cases, with a low mode 1  
654 abundance, or (3) our model is missing several pieces of essential physics, such as the  
655 microphysics of the sulfur particles, which would otherwise result in greater mode 1 abundance  
656 even when sulfur production is reduced. Option (3) is unfortunate but likely, given recent  
657 modeling results by Carlson (2010, revisions via personal communication, Sept 2<sup>nd</sup> 2013), which  
658 showed that the ratio between total sulfur mass and total sulfuric acid mass in the cloud droplets  
659 is on the order of 0.1-1%. We can calculate the same ratio for our model by adding up the masses  
660 of the bare condensation nuclei and the sulfur cores of the sulfuric acid droplets and dividing it  
661 by the mass of the sulfuric acid in the droplets. Figure 16 shows this ratio for our three sulfur  
662 production rate cases. The sulfur-to-sulfuric-acid mass ratio steadily decreases with altitude until  
663 the middle cloud, where it quickly decreases due to the turbulence in the region causing  
664 increased condensation of sulfuric acid onto the droplets; the ratio increases below the middle

665 cloud as sulfuric acid begins evaporating from the droplets. The best fit case is evidently one  
666 where the sulfur production rate is one order of magnitude less than that of our nominal case, but  
667 this contradicts figure 15, where that case did not yield enough mode 1 particles in the middle  
668 cloud to match the observations. This discrepancy may be avoided if sulfur microphysics were  
669 included in the model, as the small sulfur particles could then grow to larger sizes via  
670 condensation of sulfur vapor, perhaps to sizes comparable to that of mode 1 particles. In other  
671 words, the mass would be concentrated in mode 1 particles rather than the “sea” of smaller  
672 condensation nuclei, even for the cases with reduced sulfur production.

673 Finally, it should be noted that the periodic behavior of the nominal case disappears in the  
674 reduced sulfur cases. This is consistent with our hypothesis that the oscillation is caused by slow  
675 growth of mode 1 particles due to coagulation with the background “sea” of much smaller  
676 particles – if the “sea” is reduced, then coagulation may not be enough to allow mode 1 particles  
677 to grow past the Kelvin barrier. This further suggests that the reduced sulfur cases match the true  
678 state of the Venus clouds more closely than the nominal case, as no periodic behavior similar to  
679 those in the nominal case has yet been observed.

### 680 *3.4 Transient Wind Results*

681 Figure 17 gives the number density results before (black), immediately after (blue), and  
682 about an Earth week after a transient updraft event lasting  $\sim 14$  Earth hours ( $5 \times 10^4$  s) (red),  
683 using the wind speed profile given in Figure 6. We see that a detached haze layer forms at 75 km  
684 with a peak number density 2 orders of magnitude greater than the number density at that altitude  
685 before the wind event. The altitude of the detached haze is likely artificial given our wind profile,  
686 and the actual maximum detached haze number density is likely overestimated due to the lack of  
687 horizontal diffusion aiding (the already present) vertical diffusion in smoothing out the number

688 density profile. However, the occurrence of an increase in number density at the altitude of the  
689 turn-over should be profile-independent. In the week that follows, the detached haze layer  
690 diffuses away so that the peak number density is more than an order of magnitude lower than its  
691 maximum immediately following the wind event. This shows that such a wind event produces  
692 the right time scales for the observed haze variability from Wilquet et al. (2012), on the order of  
693 days. Furthermore, the diffusion of the detached haze particles upwards results in an increase in  
694 the number density of the UH such that there is now a much better agreement between the  
695 Wilquet et al. (2009) UH number density observations and that of our model above 80 km. It is  
696 clear, however, that the agreement between data and model would be even better if the relaxed  
697 distribution was shifted up by 10 km. This suggests that the turnover was actually 10 km higher  
698 in the actual observations, though it is unlikely that such large gusts existed at such high  
699 altitudes.

700 Figure 18 shows the size distributions at altitudes close to the detached haze layer at the  
701 same times as Figure 17. Multiple size modes form below the turnover of the wind immediately  
702 following the wind event (blue). The small mode at  $\sim 0.2 \mu\text{m}$  is largely unchanged from the  
703 equilibrium distribution for altitudes below the detached haze, but is much more abundant within  
704 the detached haze itself at 75 km; this is caused by the advection of these small particles up to  
705 the altitude of the detached haze. The “bump” associated with the high altitude tail of the mode 2  
706 cloud particles in the equilibrium distribution (black) becomes much more distinct due to upward  
707 advection of more mode 2 particles; this feature is much more prominent below the detached  
708 haze, which matches the observations of Wilquet et al. (2009) where the large UH particle mode  
709 (mode 2 cloud particles) number density drops off with altitude much faster than the small UH  
710 particle mode (mode 1 cloud particles). The small mode radii covers sizes  $< 0.6 \mu\text{m}$ , which is a

711 larger range than the Wilquet et al. (2009) result of 0.1-0.3  $\mu\text{m}$ ; the large mode radii covers the  
712 sizes between 0.6 and 1  $\mu\text{m}$ , similar to their results. Beyond 1  $\mu\text{m}$ , the particle abundance drops  
713 by over an order of magnitude, though a third mode does appear resulting from advected mode 3  
714 cloud particles; however, it is insignificant compared to the small and large modes. Above the  
715 turnover, the size distribution remains largely mono-modal.

716 Below the detached haze, the large mode becomes less distinct following the relaxation  
717 period (red), though both modes increase in number density. This is due to the sedimentation of  
718 large mode particles from the detached haze, as we see a large decrease in number density at the  
719 altitude of the detached haze itself. There is also an increase in number density above the  
720 turnover, as the detached haze particles diffuse upwards from the number density maximum.  
721 Thus, if the bimodality observed by Wilquet et al. (2009) was caused by winds, then it was likely  
722 transient in nature. This is supported by the order of magnitude variability between extinction  
723 profiles of the UH taken only days apart presented in Wilquet et al. (2012). It is unlikely that  
724 condensational and coagulation growth play any important role here, as their timescales are far  
725 greater than the observed variability timescale (James et al. 1997; Seinfeld and Pandis 2006).

726 In section 2.6 we noted the unrealistic long gust duration we have used ( $\sim 14$  Earth hours).  
727 However, we see that the UH size distribution is still visibly disturbed almost a full Earth week  
728 after the wind event in question. If we suppose that our wind event is caused by subsolar  
729 convection near  $50^\circ$  N that lasted for a full 14 hours and that the wind was constantly upwards  
730 with velocity  $\sim 1 \text{ m s}^{-1}$  at the cloud top, then given poleward meridional velocities of  $\sim 5 \text{ m s}^{-1}$   
731 (Rossow et al. 1990) (a high estimate), it would take  $\sim 1$  Earth week for this parcel of air to reach  
732  $70^\circ$  N, the latitude where the measurements of Wilquet et al. (2009) were taken. It may not be  
733 surprising then that our “relaxed” UH number density profile matches the Wilquet et al. (2009)



734 number density data so well. However, most of these assumptions are highly optimistic and it is  
735 much more likely that our results show an exaggeration of what transient winds at the cloud tops  
736 can really do to the steady state aerosol distribution.

737

#### 738 **4. SUMMARY AND CONCLUSIONS**

739 In this study we simulated the clouds and upper haze of Venus using version 3.0 of the  
740 microphysical and vertical transport model CARMA. We showed that appropriate choices of  
741 initial, boundary, and model atmospheric conditions can not only satisfactorily reproduce the  
742 number density and size distributions of the Venus clouds as seen in Pioneer Venus data  
743 (Knollenberg and Hunten 1980), including the bimodal and possible trimodal particle size  
744 spectrum and the three separate cloud layers, but also generate a quasi-periodically varying  
745 system rather than a system with a stable equilibrium distribution. The disagreements between  
746 our results and the observations – the overestimation of the particle number density and  
747 abundance of mode 2 particles in the middle cloud and the underestimation of the lower cloud  
748 and the abundance of mode 3 particles – are all within the range of variability seen in other  
749 observations, though the addition of transient gusts in the middle cloud, which would both  
750 deplete the middle cloud of particles and create a greater number of larger particles, may  
751 improve our agreement with the Pioneer Venus Sounder Probe data.

752 We also simulated the upper haze as a mixture of droplets formed from *in situ* nucleation  
753 of sulfuric acid vapor on meteoric dust and droplets upwelled from the cloud decks below. We  
754 showed that the former population rapidly coagulates with the latter population, resulting in a  
755 mono-modal size distribution. Meanwhile, for altitudes below 80 km there is good agreement  
756 between our model particle number densities and the sum of the small mode (mode 1) and large

757 mode (mode 2) number densities from Wilquet et al. (2009); above 80 km, we underestimate the  
758 number density by about half an order of magnitude. These particles are likely those originally  
759 observed by the Pioneer Venus OCPP (Kawabata et al. 1980), and could represent the haze under  
760 stable atmospheric conditions. These discrepancies were reduced upon the application of a  
761 transient updraft, which created a detached haze layer at the altitude of turnover. The diffusion of  
762 the detached haze upwards increased the particle number density of the UH such that the results  
763 agreed with the UH number densities derived by Wilquet et al. (2009) above 80 km. The  
764 resulting size distribution showed a clear bimodal structure below the detached haze immediately  
765 after the wind event, with the small mode (mode 1) particles having radii  $< 0.6 \mu\text{m}$ , and the large  
766 mode having radii between 0.6 and  $1 \mu\text{m}$ , similar to the results of Wilquet et al. (2009). The  
767 relaxation of the multi-modal structures in the size distribution back to a mono-modal  
768 distribution had a timescale of roughly an Earth week, similar to the time scales of haze  
769 variability observed by Venus Express (Luz et al. 2011, Markiewicz et al. 2007). The duration  
770 and strength of the updraft were likely exaggerations of what actually takes place in the Venus  
771 atmosphere, though subsolar convection could be a viable candidate for the generation of these  
772 events under optimistic assumptions.

773 We noted a quasi-periodic variability in our results with a rough period of  $\sim 6$  Earth  
774 months despite a stable background atmospheric state and constant input of sulfuric acid vapor  
775 and condensation nuclei. This variability is most apparent in the middle cloud, where steady  
776 coagulation of small particles ( $\sim 10 \text{ nm}$ ) with mode 1 particles lead to a slow increase in the mean  
777 mode 1 particle radii. Upon reaching the Kelvin barrier, the mode 1 particles rapidly grow to  
778 mode 2 particles via condensational growth, while upward diffusion of mode 1 particles from  
779 below replenish the mode 1 population. The cycle then repeats and a new wave of mode 2

780 particles appear; these new mode 2 particles coagulate with the old mode 2 particles, resulting in  
781 mode 3 particles that then sediment out of the model domain. This process does not occur if the  
782 sulfur condensation nuclei production rate is decreased by an order of magnitude or more, nor  
783 does it occur if the condensation nuclei are larger. Comparison between model results and  
784 Pioneer Venus observations (Knollenberg and Hunten 1980) suggests that the LCPS data may  
785 have been taken during one of the unstable “growth phases” rather than the much more long-  
786 lived stable phases. These episodic variations also leads to periodicity in the magnitude of the  
787 sulfuric acid flux out of the bottom boundary of the model domain and suggests possible sulfuric  
788 acid “rain events” that could occur immediately below the cloud deck. Such long term variability  
789 in particle population should be detectable by VIRTIS observations of the Venus night side.

790         The sulfur production rate in the upper cloud is uncertain and could be much lower than  
791 half of the sulfuric acid production rate as assumed in Imamura and Hashimoto (2001) and in our  
792 nominal model. Comparisons with sulfur-to-sulfuric-acid mass ratios of the cloud droplets  
793 derived from UV data (Carlson 2010, revisions via personal communications, Sept 2<sup>nd</sup> 2013)  
794 shows that the best fit case is one where the sulfur production rate is reduced by an order of  
795 magnitude from that of the nominal case. However, comparison of this case with LCPS particle  
796 size distributions shows that the model predicts mode 1 particle abundances in the middle cloud  
797 two orders of magnitude less what is observed. This discrepancy could be caused by the lack of  
798 sulfur microphysics in our model, which could allow the sulfur condensation nuclei to grow to  
799 mode 1 particles ( $\sim 0.2 \mu\text{m}$ ) instead of being fixed at a size of  $\sim 10 \text{ nm}$ .

800         It is necessary for future models to include both sulfur and sulfuric acid microphysics in  
801 order to provide a more complete picture of the processes occurring within the Venus clouds and  
802 hazes. Interactions between aerosols formed from these species and their gas phases are diverse

803 and only a subset has been tested. Furthermore, the production rates of these two species,  
804 particularly sulfur and its allotropes, require better constraints from both chemical models that  
805 take into account sinks due to aerosol formation and observations that are able to probe down to  
806 the altitudes where photochemistry dominates. Finally, continuous observation of the Venus  
807 hazes and clouds is essential in constraining their time evolution, especially after transient  
808 events.

809

## 810 **Acknowledgements**

811 We thank S. Garimella and R. L. Shia for assistance with the setting up and running of the  
812 CARMA code. We thank R. W. Carlson and C. Parkinson for their valuable inputs. We thank C.  
813 Li for his help in speeding up our model runs by more than a factor of 10. This research was  
814 supported in part by the Venus Express program via NASA NNX10AP80G grant to the  
815 California Institute of Technology, and in part by an NAI Virtual Planetary Laboratory grant  
816 from the University of Washington to the Jet Propulsion Laboratory and California Institute of  
817 Technology. Part of the research described here was carried out at the Jet Propulsion Laboratory,  
818 California Institute of Technology, under a contract with the National Aeronautics and Space  
819 Administration.

820

821

822 **REFERENCES**

- 823  
824 Ayers G. P., Gillett R. W., and Gras J. L. (1980) On the vapor pressure of sulfuric acid. *Geophys.*  
825 *Res. Lett.*, 7, pp. 433-436.  
826  
827 Baker R. D., Schubert G., and Jones P. W. (1998) Cloud-level penetrative compressible  
828 convection in the Venus atmosphere. *J. Atmos. Sci.*, 55, pp. 3-18.  
829  
830 Baker R. D., Schubert G., and Jones P. W. (1999) High Rayleigh number compression  
831 convection in Venus' atmosphere: Penetration, entrainment, and turbulence. *J. Geophys. Res.*,  
832 104, pp. 3815-3832.  
833  
834 Bardeen C. G., Toon O. B., Jensen E. J., Marsh D. R., and Harvey V. L. (2008) Numerical  
835 simulations of the three dimensional distribution of meteoric dust in the mesosphere and upper  
836 stratosphere. *J. Geophys. Res.*, 113, D17202, 15pp.  
837  
838 Bardeen C. G., Conley A., Jensen E., Colarco P., Toon O., Fan T., and Smith J. (2011) The  
839 CARMA 3.0 microphysics package in CESM. Whole Atmosphere Working Group Meeting.  
840  
841 Barker E. S., Woodman J. H., Perry M. A., Hapke B. A., and Nelson R. (1975) Relative  
842 spectrophotometry of Venus from 3067 to 5960 Å. *J. Atmos. Sci.*, 32, pp. 1205-1211.  
843  
844 Belton M. J. S., Smith G. R., Schubert G., and Del Genio A. D. (1976) Cloud patterns, waves and  
845 convection in the Venus atmosphere. *J. Atmos. Sci.*, 33, pp. 1394-1417.  
846  
847 Bertaux J-L., Vandaele A-C., Korablev O., Villard E., Fedorova A., Fussen D., Quemerais E.,  
848 Belyaev D., Mahieux A., Montmessin F., Muller C., Neefs E., Nevejans D., Wilquet V., Dubois J.  
849 P., Hauchecorne A., Stepanov A., Vinogradov I., Rodin A., and the SPICAV/SOIR team. (2007)  
850 A warm layer in Venus' cryosphere and high-altitude measurements of HF, HCl, H<sub>2</sub>O, and HDO.  
851 *Nature*, 450, pp. 646-649.  
852  
853 Carlson R. W., Kamp L. W., Baines K. H., Pollack J. B., Grinspoon D. H., Encrenaz Th.,  
854 Drossart P., and Taylor F. W. (1993) Variations in Venus cloud properties: A new view of Venus's  
855 cloud morphology as observed by the Galileo Near-Infrared Mapping Spectrometer. *Planet.*  
856 *Space Sci.*, 41, pp. 477-485.  
857  
858 Carlson R. W. (2010) Venus's ultraviolet absorber and sulfuric acid droplets. Paper presented at  
859 the *International Venus Conference, Aussois, France, 20-26 June 2010*.  
860  
861 Clancy R. T. and Muhleman D. O. (1991) Long-term (1979-1990) changes in the thermal,  
862 dynamical, and compositional structure of the Venus mesosphere as inferred from microwave  
863 spectral line observations of <sup>12</sup>CO, <sup>13</sup>CO, and C<sup>18</sup>O. *Icarus*, 89, pp. 129-146.  
864  
865 Crisp D., Sinton W. M., Hodapp K.-W., Ragent B., Gerbault, F., Goebel J. H., Probst R.G., Allen  
866 D. A., Pierce K., Stapelfeldt K. R. (1989) The nature of the near-infrared features on the Venus  
867 night side. *Science*, 246, pp. 506-509.

868  
869 Crisp D., Ingersoll A. P., Hildebrand C. E., and Preston R. A. (1990) VEGA Balloon  
870 meteorological measurements, *Advanc. Space Res.*, 10, pp. 109-124.  
871  
872 Crisp D., McMuldroch S., Stephens S. K., Sinton W. M., Ragent B., Hodapp K.-W., Probst R. G.,  
873 Doyle L. R., Allen D. A., and Elias J. (1991) Ground-based near-infrared imaging observations  
874 of Venus during the Galileo encounter. *Science*, 253, pp. 1538-1541.  
875  
876 English J. M., Toon O. B., Mills M. J., and Yu F. (2011) Microphysical simulations of new  
877 particle formation in the upper troposphere and lower stratosphere, *Atmos. Chem. Phys.*, 11, pp.  
878 9303-9322.  
879  
880 Esposito L. W., Knollenberg R. G., Marov M. Y., Toon O. B., and Turco R. P. (1983) In: The  
881 clouds and hazes of Venus, in *Venus*, edited by Hunten, D. M. et al., pp. 484-564. Univ. of Ariz.  
882 Press, Tucson, USA.  
883  
884 Gadsden M. (1968) Sodium in the upper atmosphere: Meteoric origin. *J. Atmos. Terr. Phys.*, 30,  
885 pp. 151-161.  
886  
887 Garate-Lopez I., Hueso R., Sanchez-Lavega A., Peralta J., Piccioni G., and Drossart P. (2013) A  
888 chaotic long-lived vortex at the southern pole of Venus. *Nat. Geosci.*, 6, pp. 254-257.  
889  
890 Giauque W. F., Hornung E. W., Kunzler J. E., and Rubin T. R. (1959) The thermodynamic  
891 properties of aqueous sulfuric acid solutions and hydrates from 15 to 300 K. *J. Amer. Chem. Soc.*,  
892 82, pp. 62-70.  
893  
894 Grinspoon D. H., Pollack J. B., Sitton B. R., Carlson R. W., Kamp L. W., Baines K. H., Encrenaz  
895 Th., and Taylor F. W. (1993) Probing Venus's cloud structure with Galileo NIMS. *Planet. Space  
896 Sci.*, 41, pp. 515-542.  
897  
898 Hueso R., Sanchez-Lavega A., Piccioni G., Drossart P., Gerard J. C., Khatuntsev I., Zasova L.,  
899 and Migliorini A. (2008) Morphology and dynamics of Venus oxygen airglow from Venus  
900 Express/Visible and Infrared Thermal Imaging Spectrometer observations. *J. Geophys. Res.*, 113,  
901 E00B02, 7pp.  
902  
903 Hunten D. M., Turco R. P., and Toon O. B. (1980) Smoke and dust particles of meteoric origin in  
904 the mesosphere and stratosphere. *J. Atmos. Sci.*, 37, pp. 1342-1357.  
905  
906 Ignatiev N. I., Moroz V. I., Moshkin B. E., Ekonomov V. I., Gnedykh A. V., Grigoriev A. V., and  
907 Khatuntsev I. V. (1997) Water vapour in the lower atmosphere of Venus: A new analysis of  
908 optical spectra measured by entry probes. *Planet. Space Sci.*, 45, pp. 427-438.  
909  
910 Imamura T. (1997). Momentum balance of the Venusian midlatitude mesosphere. *J. Geophys.  
911 Res.*, 102, pp. 6615-6620.  
912  
913 Imamura T. and Hashimoto G. L. (2001) Microphysics of Venusian clouds in rising tropical air.

914 *J. Atmos. Sci.*, 58, pp. 3597-3612.  
915  
916 Ingersoll A. P., Crisp D., and the VEGA Balloon Science Team. (1987) Estimates of convective  
917 heat fluxes and gravity wave amplitudes in the Venus middle cloud layer from VEGA balloon  
918 measurements. *Advanc. Space Res.*, 7, pp. 343-349.  
919  
920 Jacobson M. Z. and Turco R. P. (1994) Modeling coagulation among particles of different  
921 composition and size. *Atmos. Environ.*, 28, pp. 1327-1338.  
922  
923 James E. P., Toon O. B., and Schubert G. (1997) A numerical microphysical model of the  
924 condensational Venus cloud. *Icarus*, 129, pp. 147-171.  
925  
926 Kalashnikova O., Horanyi M., Thomas G. E., and Toon O. B. (2000) Meteoric smoke production  
927 in the atmosphere. *Geophys. Res. Lett.*, 27, pp. 3293-3296.  
928  
929 Kawabata K., Coffeen D. L., Hansen J. E., Lane W. A., Sato M., and Travis L. D. (1980) Cloud  
930 and haze properties from Pioneer Venus polarimetry. *J. Geophys. Res.*, 85, pp. 8129-8140.  
931  
932 Knollenberg R. G. and Hunten D. M. (1980) The microphysics of the clouds of Venus: Results of  
933 the Pioneer Venus particle size spectrometer experiment. *J. Geophys. Res.*, 85, pp. 8039-8058.  
934  
935 Kolodner M. A. and Steffes P. G. (1998) The microwave absorption and abundance of sulfuric  
936 acid vapor in the Venus atmosphere based on new laboratory measurements. *Icarus*, 132, pp.  
937 151-169.  
938  
939 Krasnopolsky V. A. (1983) In: Venus spectroscopy in the 3000-8000 A region by Veneras 9 and  
940 10, in *Venus*, edited by Hunten, D. M. et al., pp. 459-483. Univ. of Ariz. Press, Tucson, USA.  
941  
942 Krasnopolsky V. A. and Parshev V. A. (1983) In: Photochemistry of the Venus atmosphere, in  
943 *Venus*, edited by Hunten, D. M. et al., pp. 431-458. Univ. of Ariz. Press, Tucson, USA.  
944  
945 Krasnopolsky V. A. and Pollack J. B. (1994) H<sub>2</sub>O - H<sub>2</sub>SO<sub>4</sub> system in Venus' clouds and OCS,  
946 CO, and H<sub>2</sub>SO<sub>4</sub> profiles in Venus' troposphere. *Icarus*, 109, pp. 58-78.  
947  
948 Kulmala M. and Laaksonen A. (1990) Binary nucleation of water-sulfuric acid system:  
949 Comparison of classical theories with different H<sub>2</sub>SO<sub>4</sub> saturation vapor pressures. *J. Chem.*  
950 *Phys.*, 93, pp. 696-701.  
951  
952 Luz D., Berry D. L., Piccioni G., Drossart P., Politi R., Wilson C. F., Erard S., and Nuccilli F.  
953 (2011) Venus's southern polar vortex reveals precessing circulation. *Science*, 332, pp. 577-580.  
954  
955 Lyons J. R. (2008) An estimate of the equilibrium speciation of sulfur vapor over solid sulfur and  
956 implications for planetary atmospheres. *J. Sulfur Chem.*, 29, pp. 269-279.  
957  
958 Markiewicz W. J., Titov D. V., Limaye S. S., Keller H. U., Ignatiev N., Jaumann R., Thomas N.,  
959 Michalik H., Moissl R., and Russo P. (2007) Morphology and dynamics of the upper cloud layer

960 of Venus. *Nature*, 450, pp. 633-636.

961

962 McGouldrick K. and Toon O. B. (2007) An investigation of possible causes of the holes in the  
963 condensational Venus cloud using a microphysical cloud model with a radiative-dynamical  
964 feedback. *Icarus*, 191, pp. 1-24.

965

966 McGouldrick K., Toon O. B., and Grinspoon D. H. (2011) Sulfuric acid aerosols in the  
967 atmosphere of the terrestrial planets. *Planet. Space Sci.*, 59, pp. 934-941.

968

969 Mills F. P., Esposito L. W., Yung Y. L. (2007) In: Atmospheric composition, chemistry, and  
970 clouds, in *Exploring Venus as a Terrestrial Planet*, edited by Esposito, L. W. et al., pp. 73-100.  
971 American Geophysical Union, Washington D.C., USA.

972

973 Mills M. J. (1996) Stratospheric sulfate aerosol: A microphysical model. PhD thesis at the  
974 University of Colorado, Department of Astrophysical, Planetary, and Atmospheric sciences.

975

976 Rossow W. B., Del Benio A. D., and Eichler T. (1990) Cloud-tracked winds from Pioneer Venus  
977 OCPP images. *J. Atmos. Sci.*, 47, pp. 2053-2084.

978

979 Sabinina L. and Turpugow L. (1935) The surface tension of the system sulfuric acid-water. *Z.*  
980 *Phys. Chem.*, A173, pp. 237-241.

981

982 Sandor B. J., Clancy R. Todd, and Moriarty-Schieven G. (2012) Upper limits for H<sub>2</sub>SO<sub>4</sub> in the  
983 mesosphere of Venus. *Icarus*, 217, pp. 839-844.

984

985 Saunders R. W., Dhomse S., Tian W. S., Chipperfield M. P., and Plane J. M. C. (2012)  
986 Interactions of meteoric smoke particles with sulphuric acid in the Earth's stratosphere. *Atmos.*  
987 *Chem. Phys.*, 12, pp. 4387-4398.

988

989 Schubert G., Covey C., Del Genio A., Elson L. S., Keating G., Seiff A., Young R. E., Apt J.,  
990 Counselman III, C., Kliore A. J., Limaye S. S., Revercomb H. E., Sromovsky L. A., Suomi V. E.,  
991 Taylor F., Woo R., and von Zahn U. (1980) Structure and circulation of the Venus atmosphere. *J.*  
992 *Geophys. Res.*, 85, pp. 8007-8025.

993

994 Seiff A., Kirk D. B., Young R. E., Blanchard R. C., Findlay J. T., Kelly G. M., and Sommer S. C.  
995 (1980) Measurements of thermal structure and thermal contrasts in the atmosphere of Venus and  
996 related dynamical observations: Results from the four Pioneer Venus probes. *J. Geophys. Res.*,  
997 85, pp. 7903-7933.

998

999 Seiff A., Schofield J. T., Kliore A. J., Taylor F. W., Limaye S. S., Revercomb H. E., Sromovsky  
1000 L. A., Kerzhanovich V. V., Moroz V. I., and Marov M. Ya. (1985) Models of the structure of the  
1001 atmosphere of Venus from the surface to 100 kilometers altitude. *Adv. Space Res.*, 5, pp. 3-58.

1002

1003 Seinfeld J. H. and Pandis S. N. (2006) In: *Atmospheric chemistry and physics: From air*  
1004 *pollution to climate change, 2<sup>nd</sup> edition*. John Wiley & Sons, Inc. Hoboken, New Jersey, USA.

1005



1006 Tabazadeh A., Toon O. B., Clegg S. L., and Hamill P. (1997) A new parameterization of H<sub>2</sub>SO<sub>4</sub>/  
1007 H<sub>2</sub>O aerosol composition: Atmospheric implications. *Geophys. Res. Lett.*, 24, pp. 1931-1934.  
1008

1009 Tellmann S., Patzold M., Hausler B., Bird M. K., and Tyler G. L. (2009) Structure of the Venus  
1010 neutral atmosphere as observed by the Radio Science experiment VeRa on Venus Express. *J.*  
1011 *Geophys. Res.* 114, E00B36, 19pp.  
1012

1013 Titov D. V., Markiewicz W. J., Ignatiev N. I., Song L., Limaye S. S., Sanchez-Lavega A.,  
1014 Hesemann J., Almeida M., Roatsch T., Matz K-D., Scholten F., Crisp D., Esposito L. W., Hviid  
1015 S. F., Jaumann R., Keller H. U., and Moissl R. (2012) Morphology of the cloud tops as observed  
1016 by the Venus Express Monitoring Camera. *Icarus*, 217, pp. 682-701.  
1017

1018 Toon O. B., Turco R. P., and Pollack J. B. (1982) The ultraviolet absorber on Venus: Amorphous  
1019 sulfur. *Icarus*, 51, pp. 358-373.  
1020

1021 Toon O. B., Ragent B., Colburn D., Blamont J., and Cot C. (1984) Large, solid particles in the  
1022 clouds of Venus: Do they exist? *Icarus*, 57, pp. 143-160.  
1023

1024 Toon O. B., Turco R. P., Westphal D., Malone R., and Liu M. S. (1988) A multidimensional  
1025 model for aerosols: Description of computational analogs. *J. Atmos. Sci.*, 45, pp. 2123-2143.  
1026

1027 Toon O. B., Turco R. P., Jordan J., Goodman J., and Ferry G. (1989) Physical processes in polar  
1028 stratospheric ice clouds. *J. Geophys. Res.*, 94, pp. 11359-11380.  
1029

1030 Turco R. P., Hamill P., Toon O. B., Whitten R. C., and Kiang C. S. (1979) A one-dimensional  
1031 model describing aerosol formation and evolution in the stratosphere: I. Physical processes and  
1032 mathematical analogs. *J. Atmos. Sci.*, 36, pp. 699-717.  
1033

1034 Turco R. P., Toon O. B., Whitten R. C., and Keesee R. G. (1983) Venus: Mesospheric hazes of  
1035 ice, dust, and acid aerosols. *Icarus*, 53, pp. 18-25.  
1036

1037 White F. M. (1991) In: *Viscous Fluid Flow*. McGraw-Hill, New York, USA.  
1038

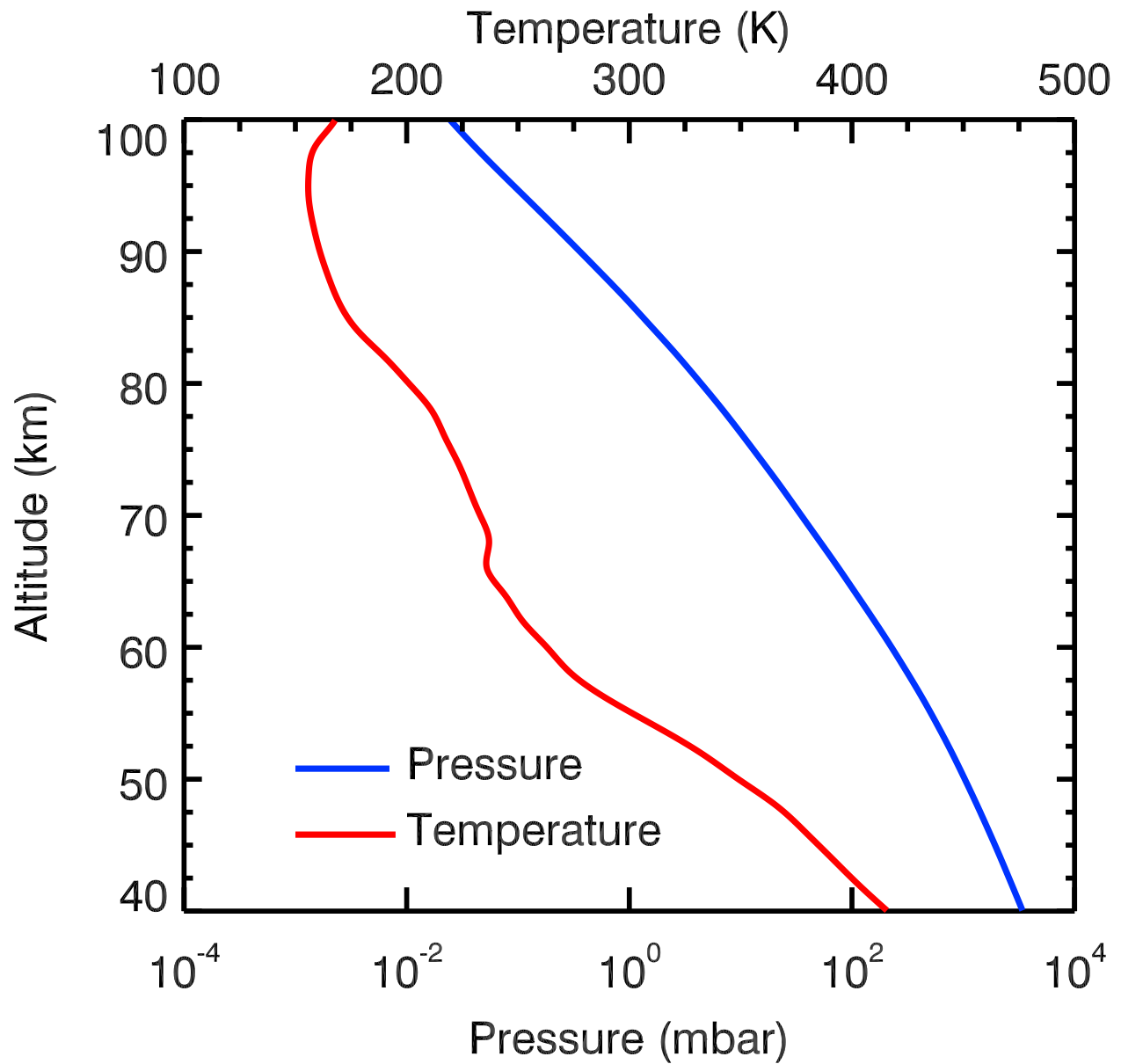
1039 Wilquet V., Drummond R., Mahieux A., Robert S., Vandaele A. C., and Bertaux J.-L. (2012)  
1040 Optical extinction due to aerosols in the upper haze of Venus: Four years of SOIR/VEX  
1041 observations from 2006 to 2010. *Icarus*, 217, pp. 875-881.  
1042

1043 Wilquet V., Fedorova A., Montmessin F., Drummond R., Mahieux A., Vandaele A. C., Villard E.,  
1044 Korablev O., and Bertaux J.-L. (2009) Preliminary characterization of the upper haze by  
1045 SPICAV/SOIR solar occultation in UV to mid-IR onboard Venus Express. *J. Geophys. Res.*, 114,  
1046 E00B42, 13pp.  
1047

1048 Yamamoto M. and Tanaka H. (1998) The Venusian Y-shaped cloud pattern based on an aerosol-  
1049 transport model. *J. Atmos. Sci.*, 55, pp. 1400-1426.  
1050

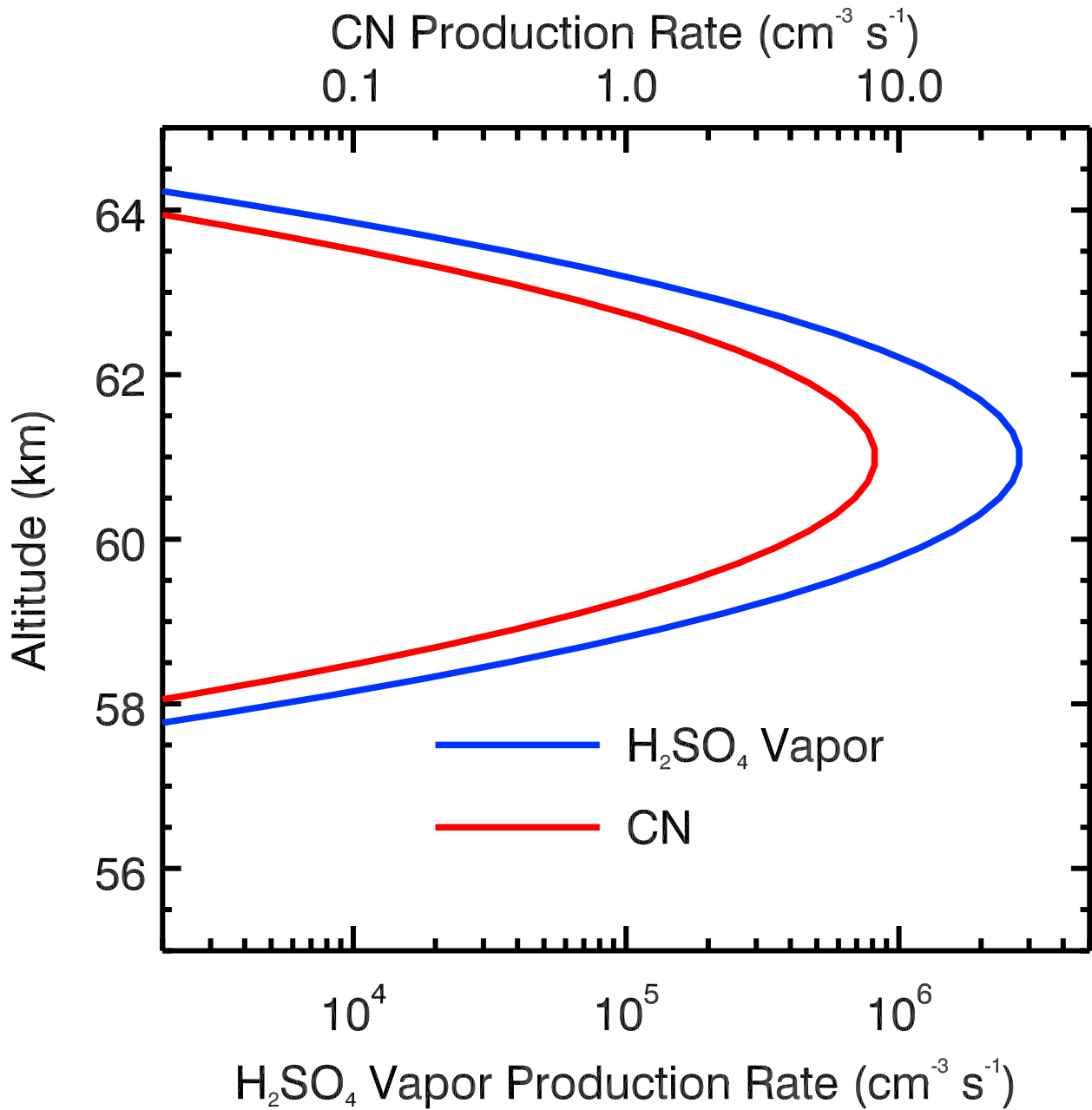
1051 Yamamoto M. and Takahashi M. (2006) An aerosol transport model based on a two-moment

1052 microphysical parametrization in the Venus middle atmosphere: Model description and  
1053 preliminary experiments. *J. Geophys. Res.*, 111, E08002, 12pp.  
1054  
1055 Young A. T. (1983) Venus cloud microphysics. *Icarus*, 56 pp. 568-577.  
1056  
1057 Yung Y. L. and DeMore W. B. (1982) Photochemistry of the stratosphere of Venus: Implications  
1058 for atmospheric evolution. *Icarus*, 51, pp. 199-247.  
1059  
1060 Zhang X., Liang M. C., Montmessin F., Bertaux J. L., Parkinson C., and Yung Y. L. (2010)  
1061 Photolysis of sulphuric acid as the source of sulphur oxides in the mesosphere of Venus. *Nat.*  
1062 *Geosci.*, 3, pp. 834-837.  
1063  
1064 Zhang X., Liang M. C., Mills F. P., Belyaev D., and Yung Y. L. (2012a) Sulfur chemistry in the  
1065 middle atmosphere of Venus. *Icarus*, 217, pp. 714-739.  
1066  
1067 Zhang X., Pandis S. N., and Seinfeld J. H. (2012b) Diffusion-limited versus quasi-equilibrium  
1068 aerosol growth. *Aerosol Sci. Tech.*, 46, pp. 874-885.  
1069



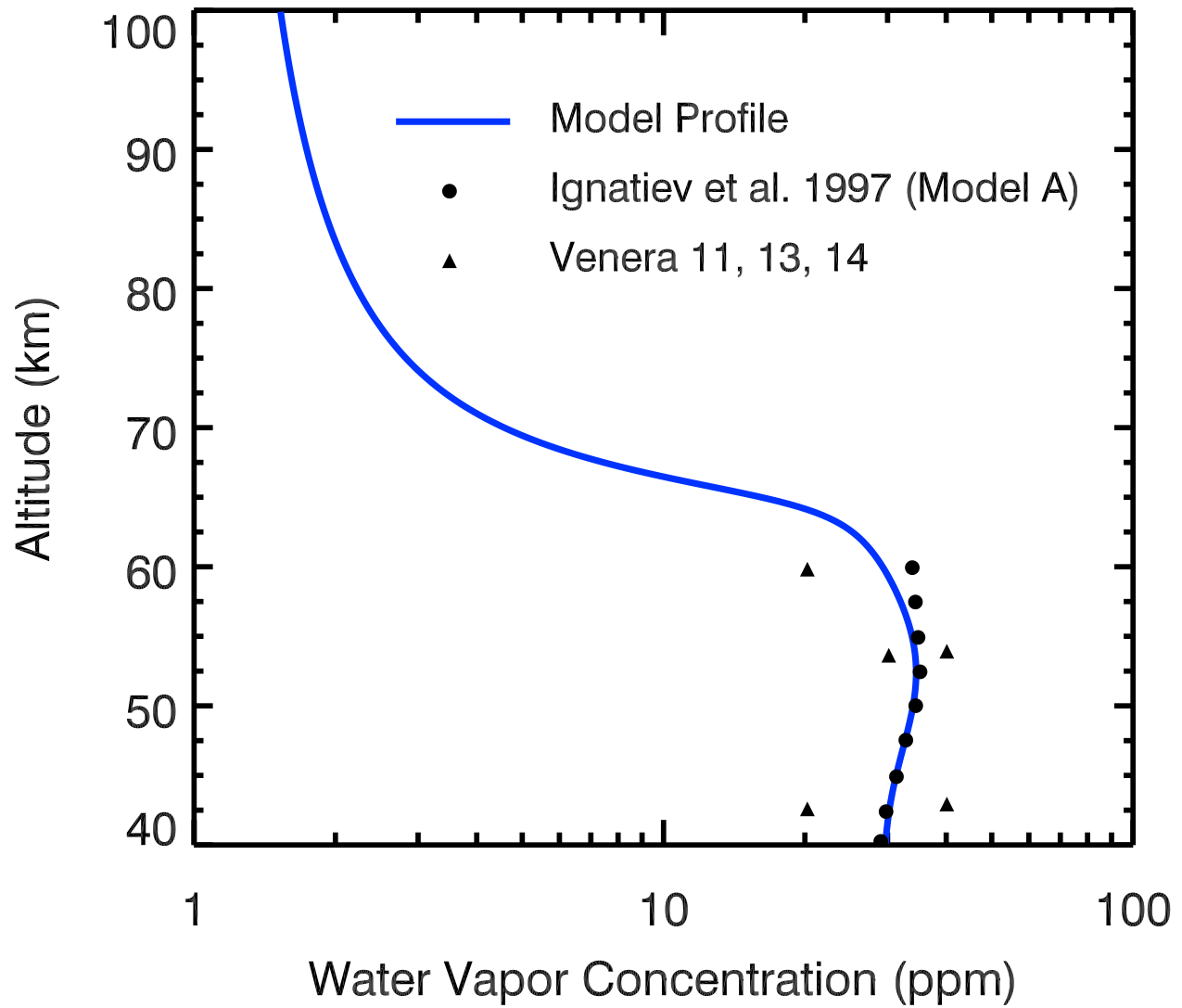
1070  
 1071  
 1072  
 1073  
 1074

Figure 1. Model temperature (red) and pressure (blue) profiles taken from the Venus International Reference Atmosphere (Seiff et al. 1985).



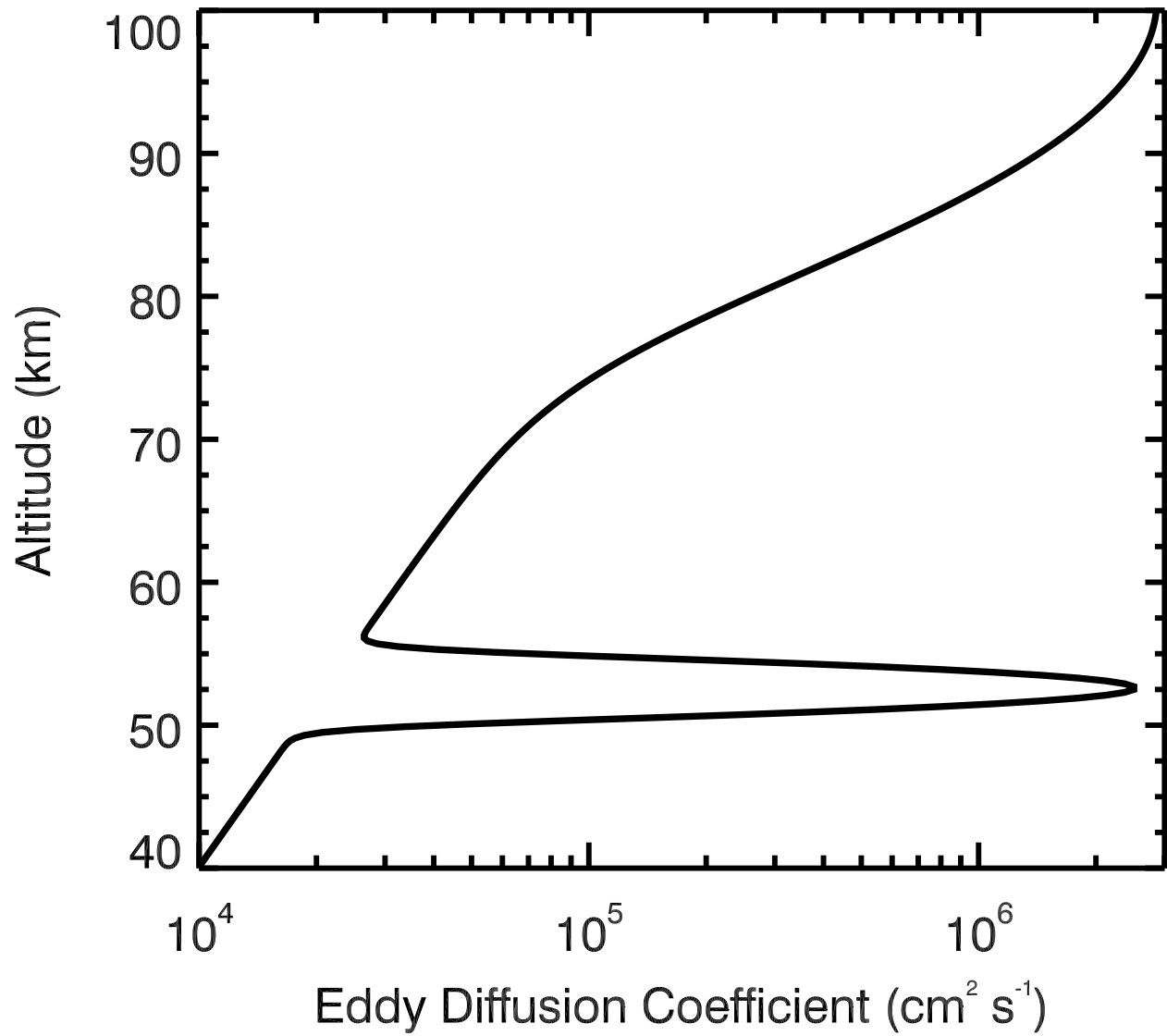
1075  
 1076  
 1077  
 1078  
 1079  
 1080  
 1081  
 1082  
 1083

Figure 2. Model production rate profiles for sulfuric acid vapor (blue) and photochemical condensation nuclei (red), based on that of Imamura and Hashimoto (2001) with the peak rates adjusted to fit LCPS data.



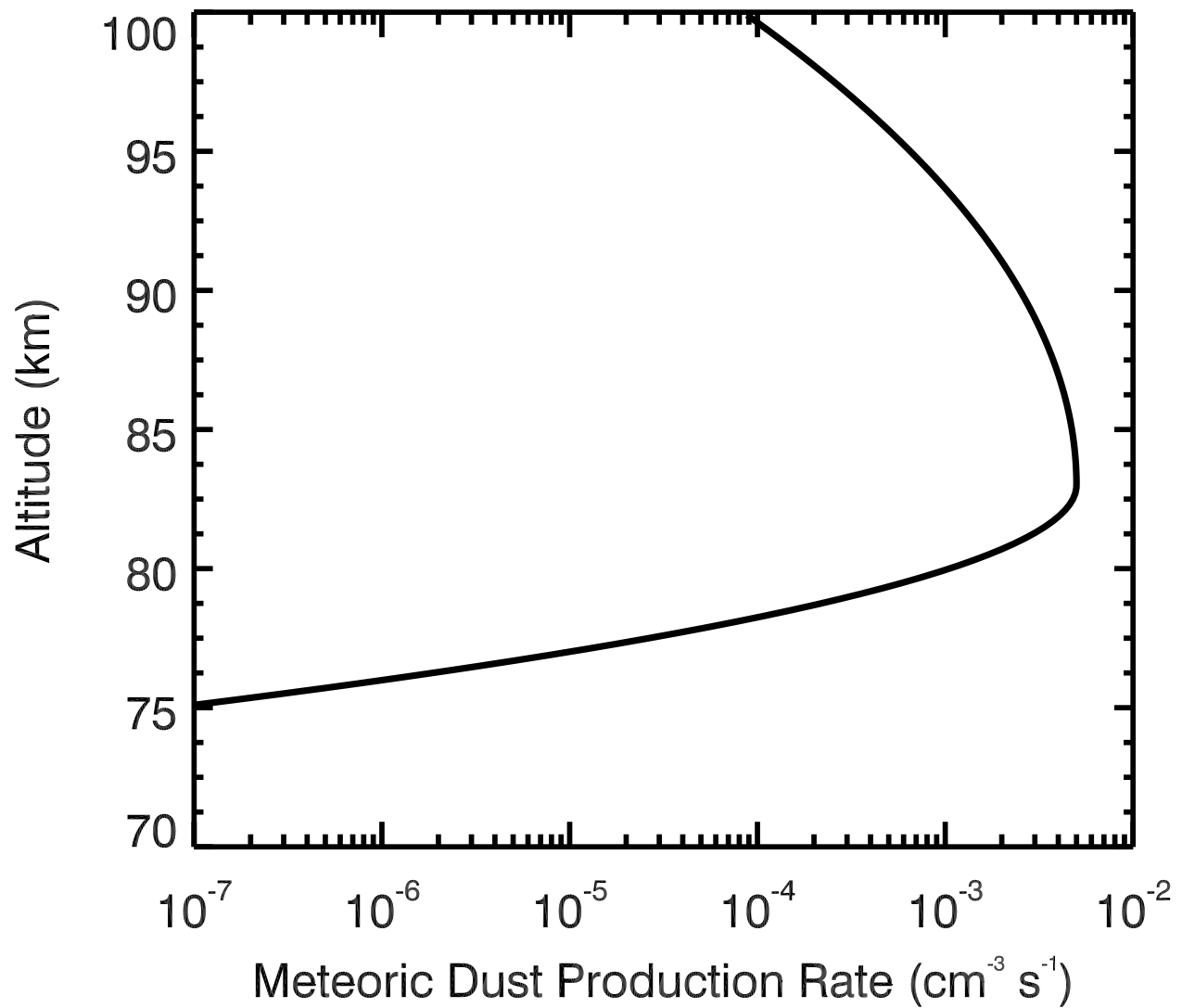
1084  
 1085  
 1086  
 1087  
 1088  
 1089  
 1090  
 1091  
 1092

Figure 3. Model water vapor profile (blue) plotted with the Model A (filled circles) and Venera 11, 13, and 14 data (triangles) from Ignatiev et al. (1997). The water vapor concentration in the upper haze is taken to be ~1 ppm from observations by Bertaux et al. (2007).



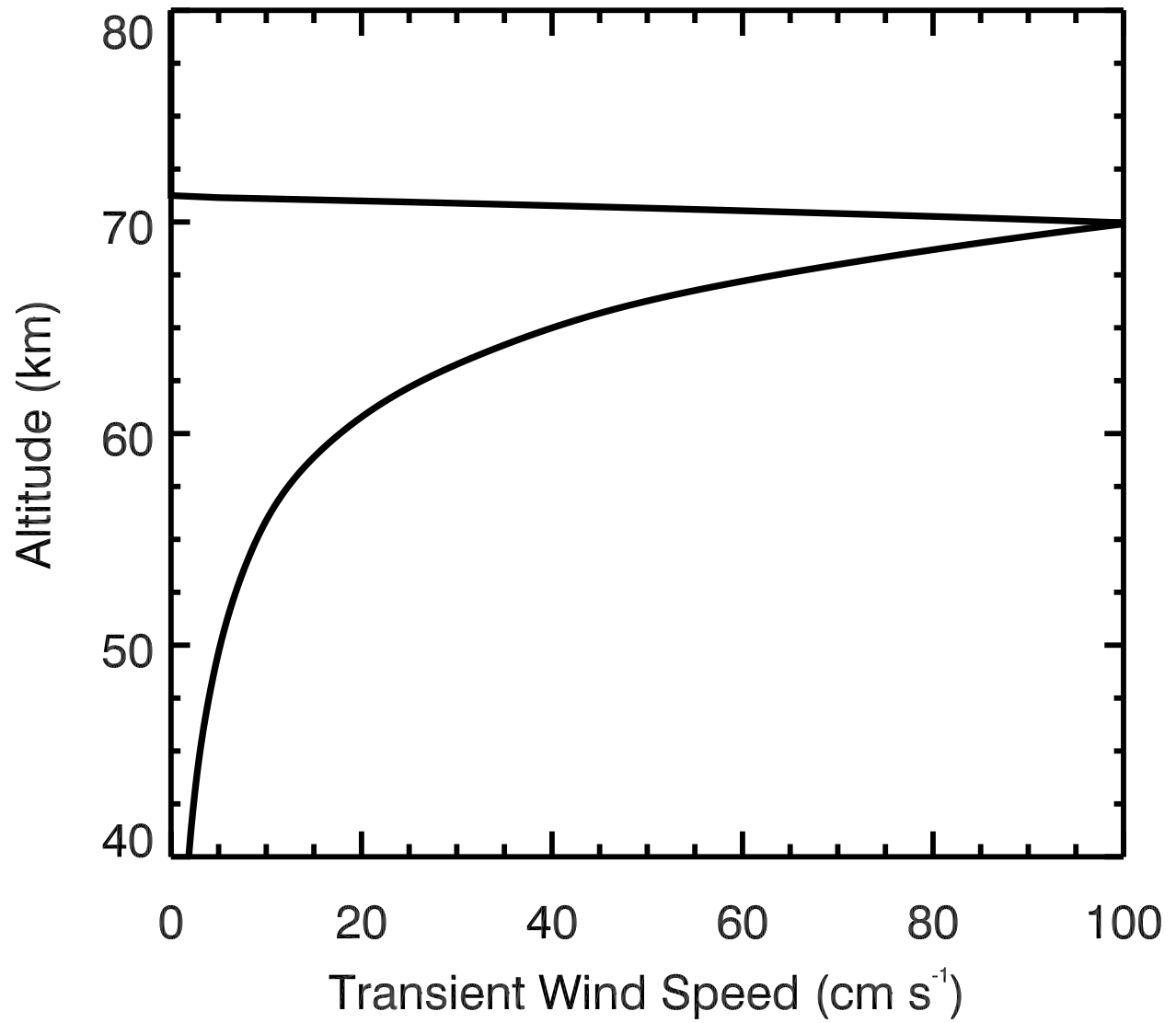
1093  
1094  
1095  
1096  
1097  
1098

Figure 4. Model eddy diffusion coefficient profile, with the 40-70 km section based on Imamura and Hashimoto (2001), and the 70-100 km section based on Krasnopolsky (1983).



1099  
 1100  
 1101  
 1102  
 1103  
 1104  
 1105  
 1106  
 1107

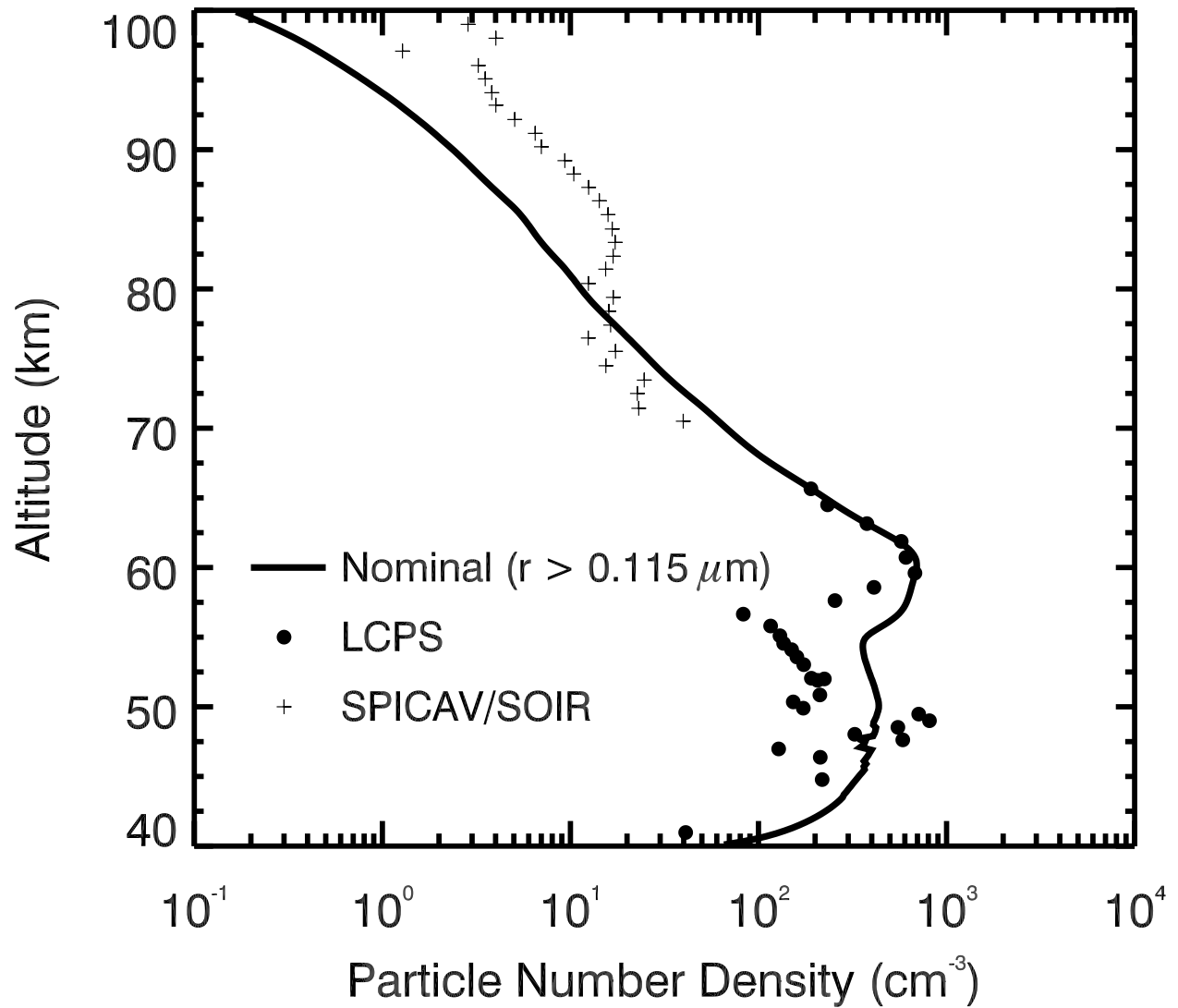
Figure 5. Model meteoric dust production rate profile, based on Kalashnikova et al. (2000), normalized to 1.3 nm particles, and shifted down from the original distribution by 4 km in order for the maximum of this profile to match that of the number density profile of the small mode particles in the UH, as retrieved from solar occultation data by Wilquet et al. (2009).



1108  
1109  
1110  
1111  
1112  
1113

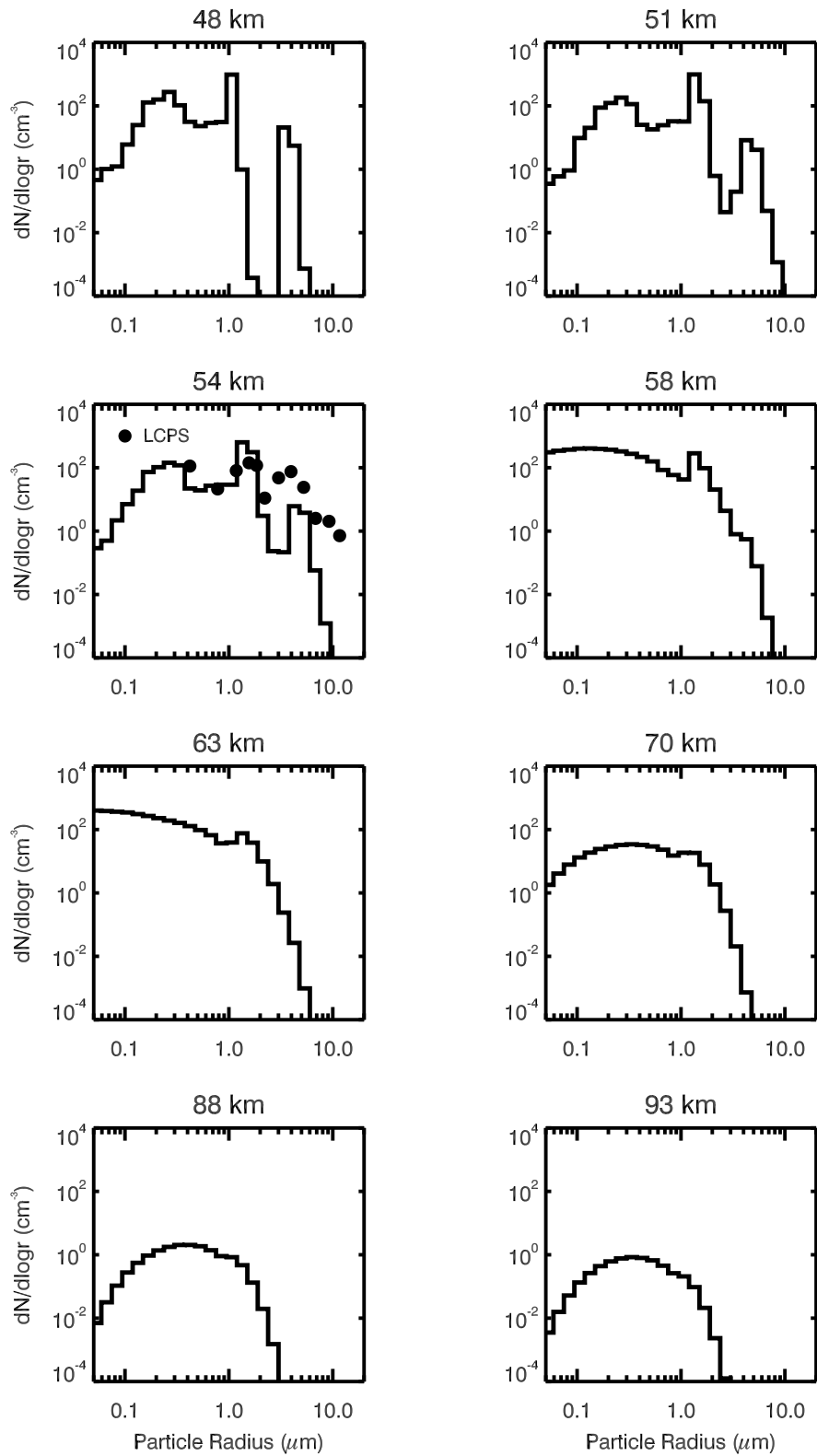
Figure 6. Model wind speed profile with the portion below 70 km taken from Imamura and Hashimoto (2001), and the cut-off above 70 km representing the turning over of the upwelling.





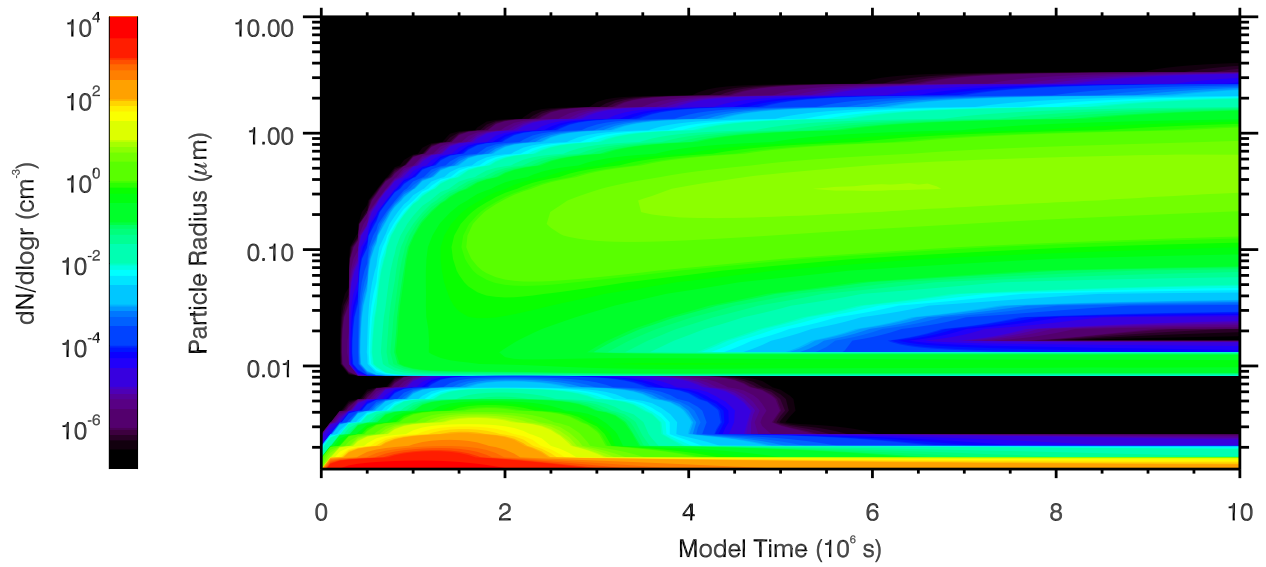
1114  
 1115  
 1116  
 1117  
 1118  
 1119  
 1120

Figure 7. Number density of cloud and haze particles with radius  $r > 0.115 \mu\text{m}$  (solid line) from the nominal model compared to total number density data from LCPS (filled circles) (Knollenberg and Hunten 1980) and Venus Express (pluses) (Wilquet et al. 2009).



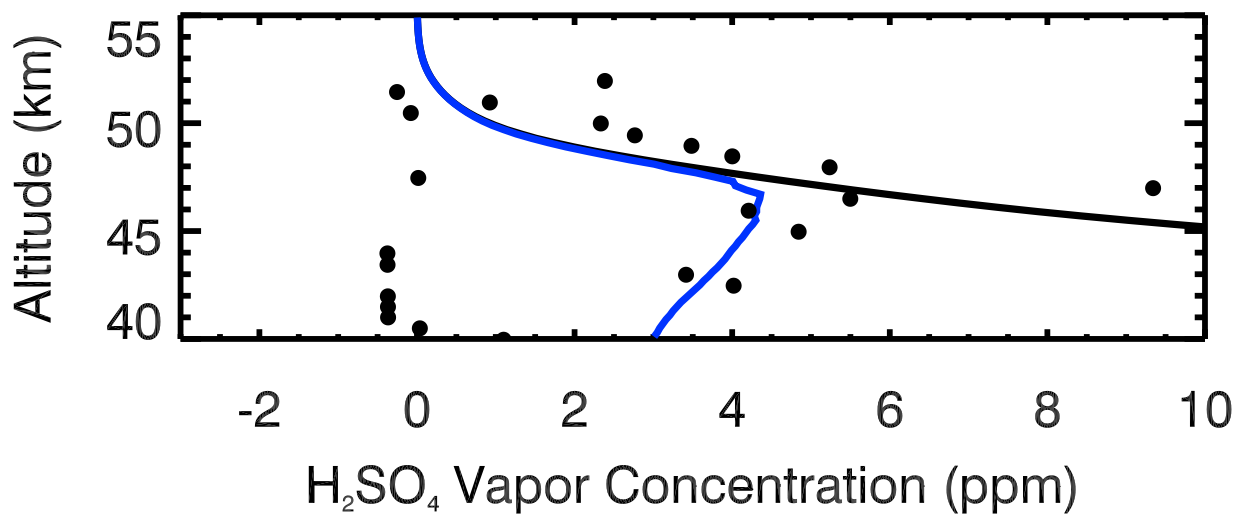
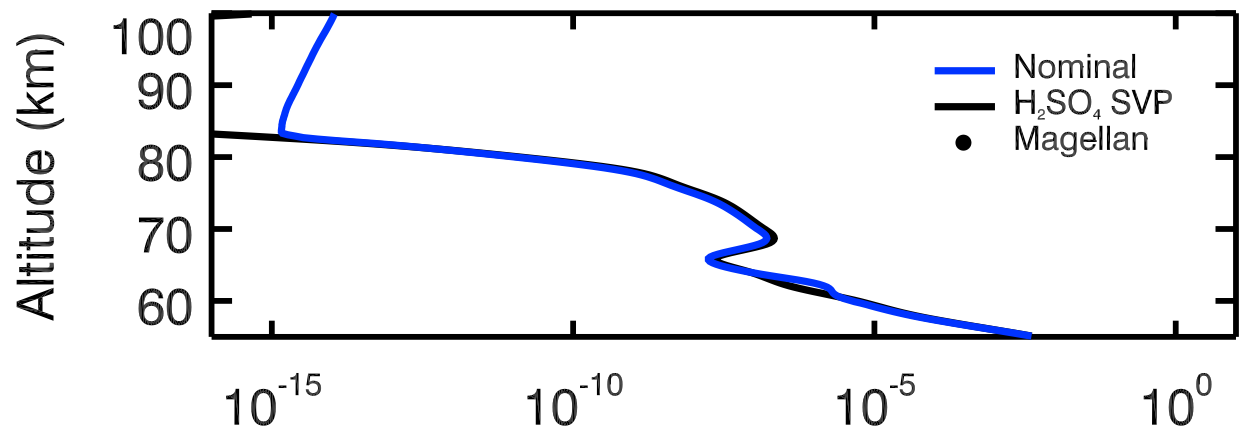
1121  
 1122  
 1123  
 1124  
 1125

Figure 8. Particle size distributions at various altitudes from the nominal model. LCPS size data at 54.2 km (dots) (Knollenberg and Hunten 1980) is plotted for comparison.



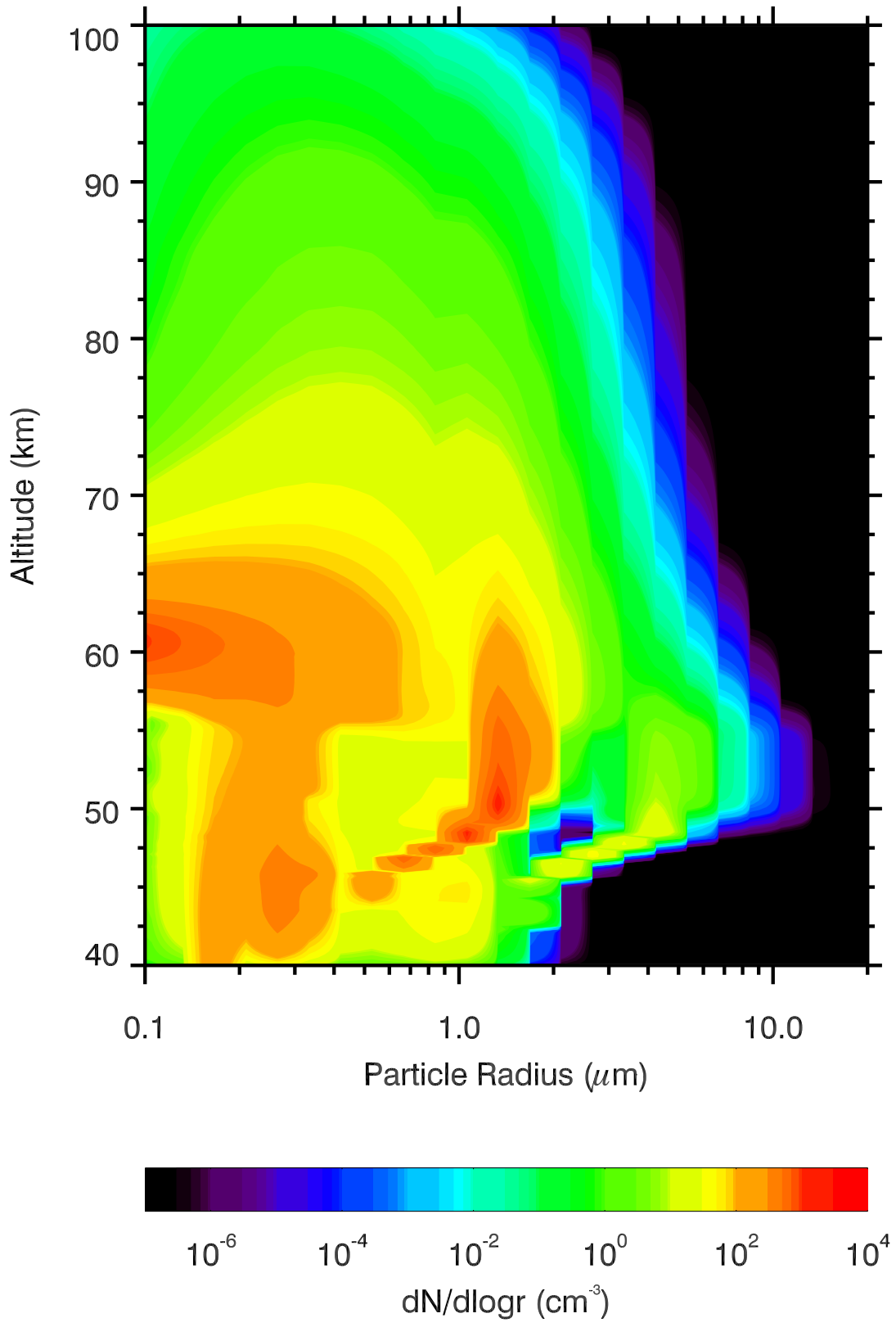
1126  
 1127  
 1128  
 1129  
 1130  
 1131  
 1132  
 1133  
 1134

Figure 9. Time evolution of the UH particle size distribution at 84 km at the beginning of the nominal model run, from  $t = 0$  to  $t = 10^7$  s. The green “bar” at 10 nm is a result of the artificial injection of 10 nm particles into the model domain as photochemical condensation nuclei and should be ignored. The black regions represent parts of the phase space where  $dN/d\log r < 10^{-7}$   $\text{cm}^{-3}$ .



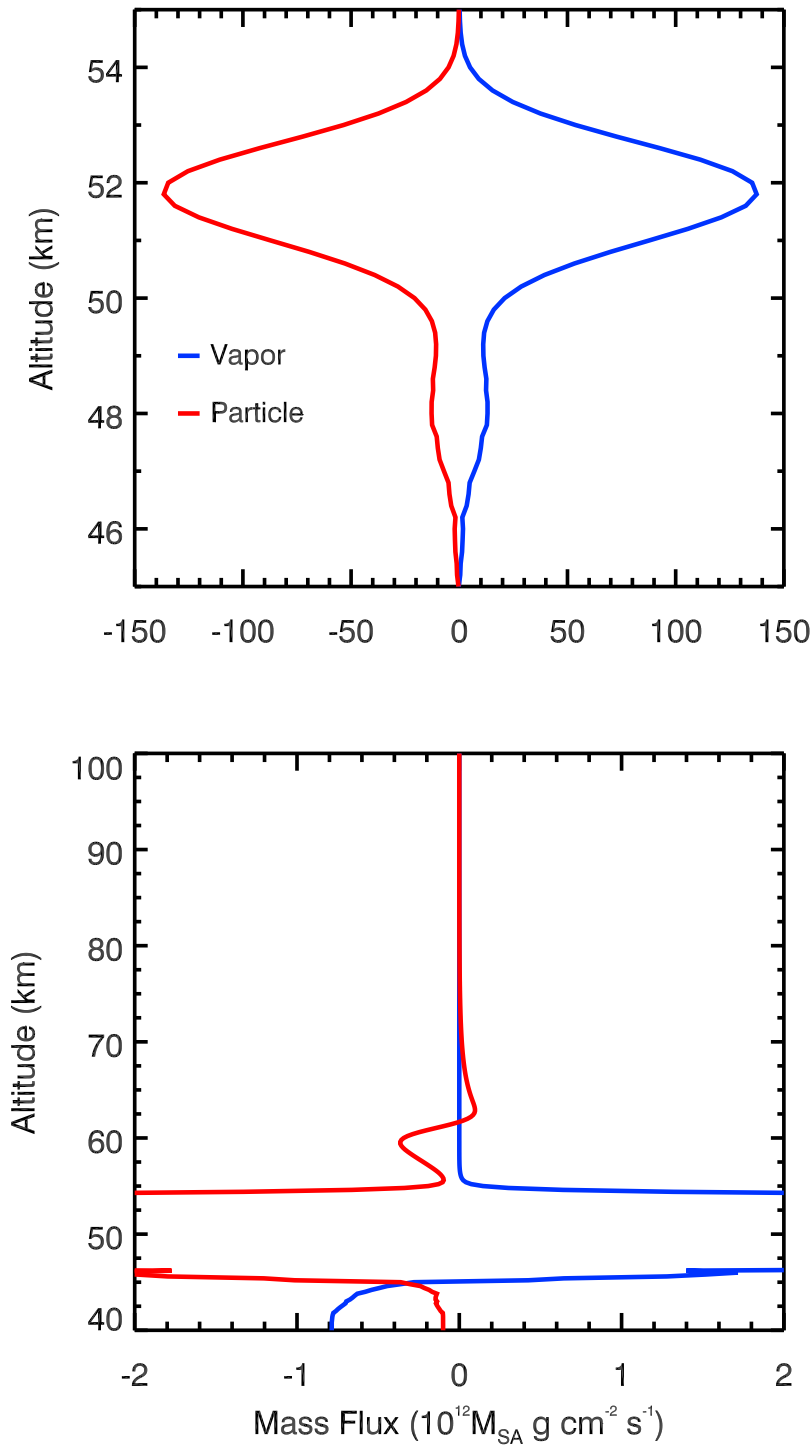
1135  
 1136  
 1137  
 1138  
 1139  
 1140  
 1141

Figure 10. Sulfuric acid vapor mixing ratio from the nominal model (blue) compared with the sulfuric acid saturation vapor pressure over a flat surface (black) (sec. 2.2) and Magellan radio occultation data analyzed by Kolodner and Steffes (filled circles) (1998).



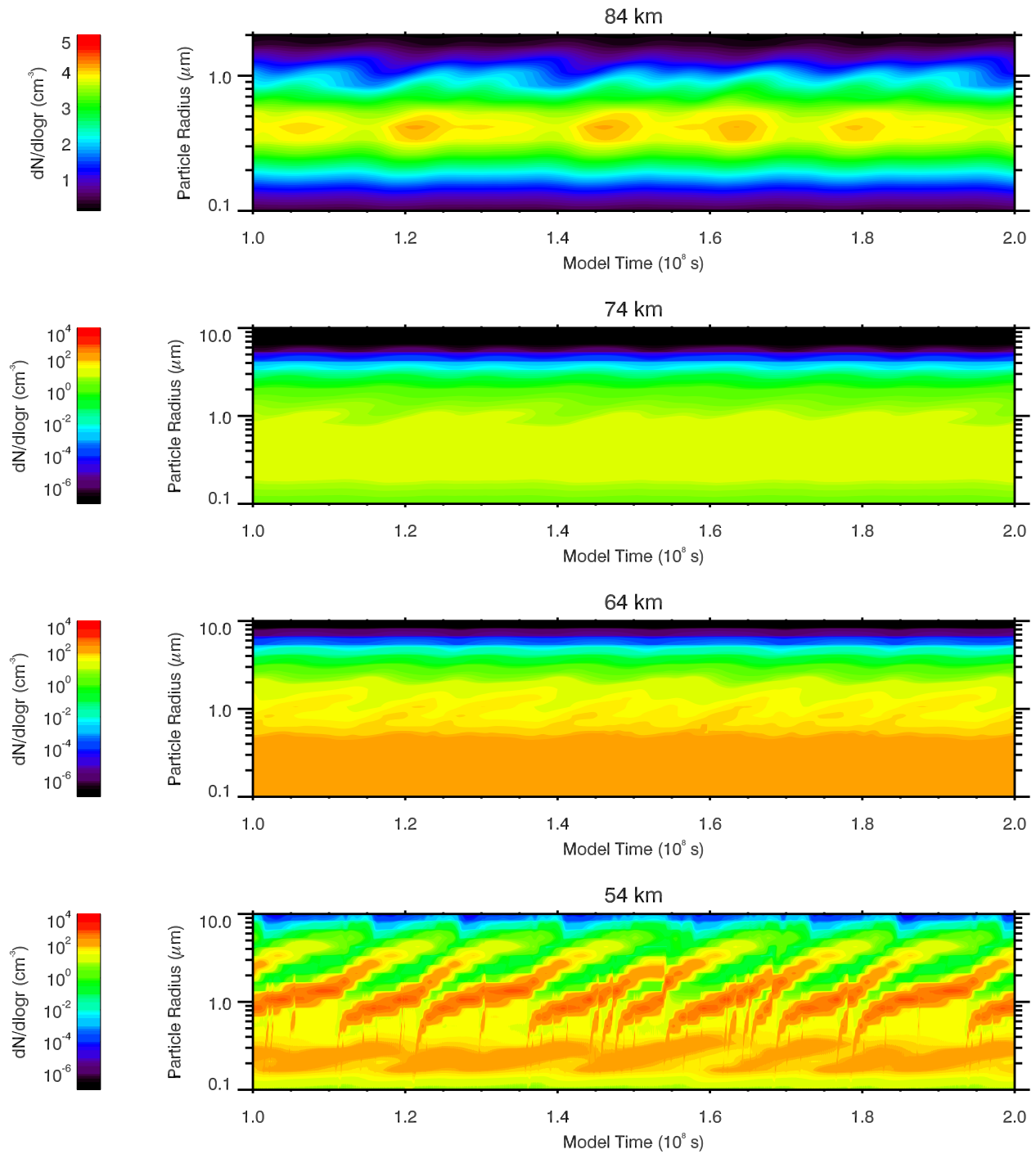
1142  
 1143  
 1144  
 1145

Figure 11. The nominal particle number density as a function of particle size and altitude. The black regions represent parts of the phase space where  $\text{dN}/\text{dlogr} < 10^{-7} \text{ cm}^{-3}$ .



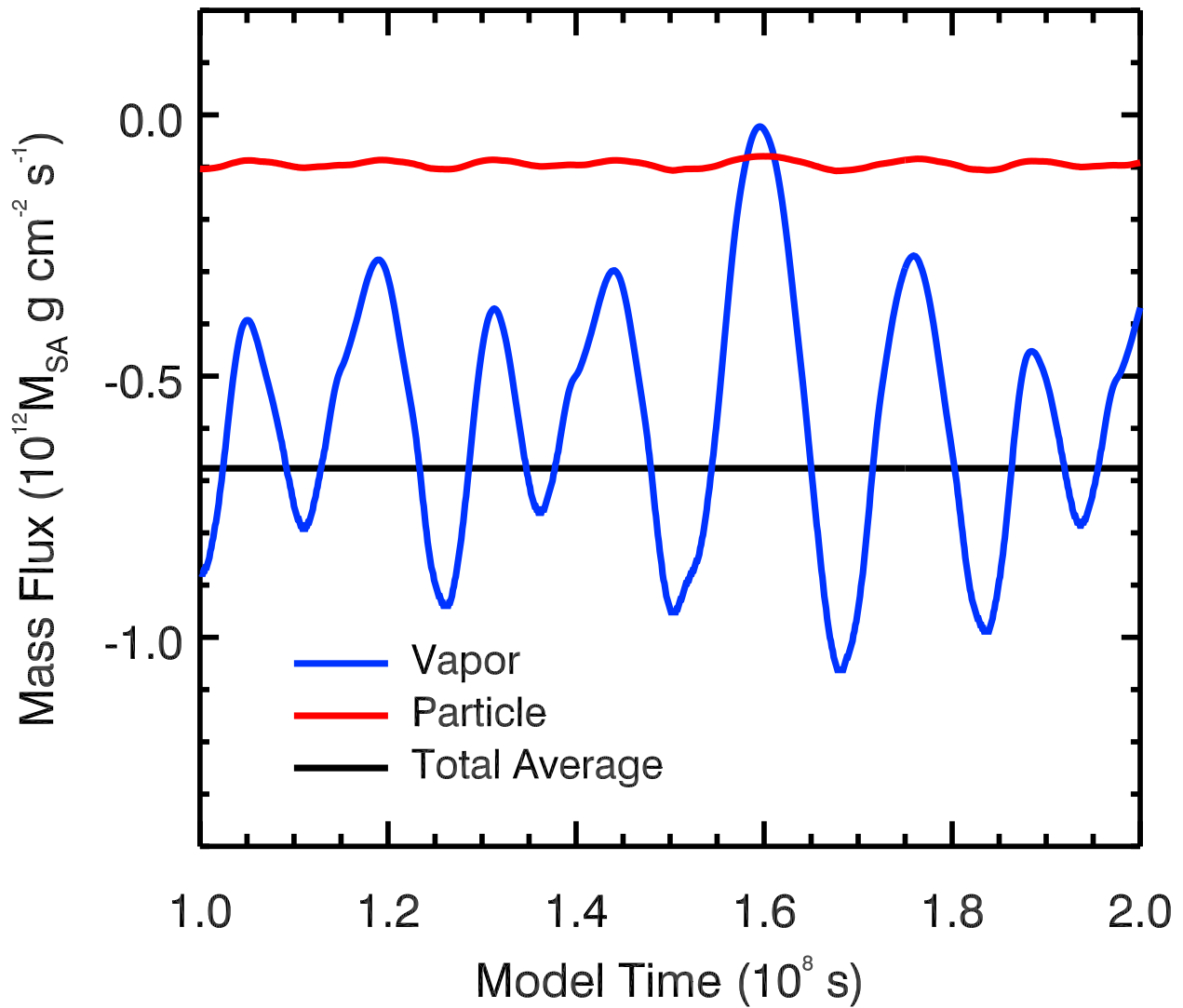
1146  
 1147  
 1148  
 1149  
 1150  
 1151  
 1152  
 1153

Figure 12. The nominal sulfuric acid vapor (blue) and particle (red) mass fluxes at steady state at the same time step as in figures 7, 8, 10, and 11 expressed in units of mass equivalent to  $10^{12}$  sulfuric acid molecules per unit area per second, where each molecule has mass  $M_{SA} \sim 1.6 \times 10^{-22}$  g. Note the different axes scales between the top and bottom panels: the top panel shows the high flux values of the middle cloud, while the bottom panel shows the lower flux values at the other altitudes.



1154  
 1155  
 1156  
 1157  
 1158  
 1159  
 1160  
 1161

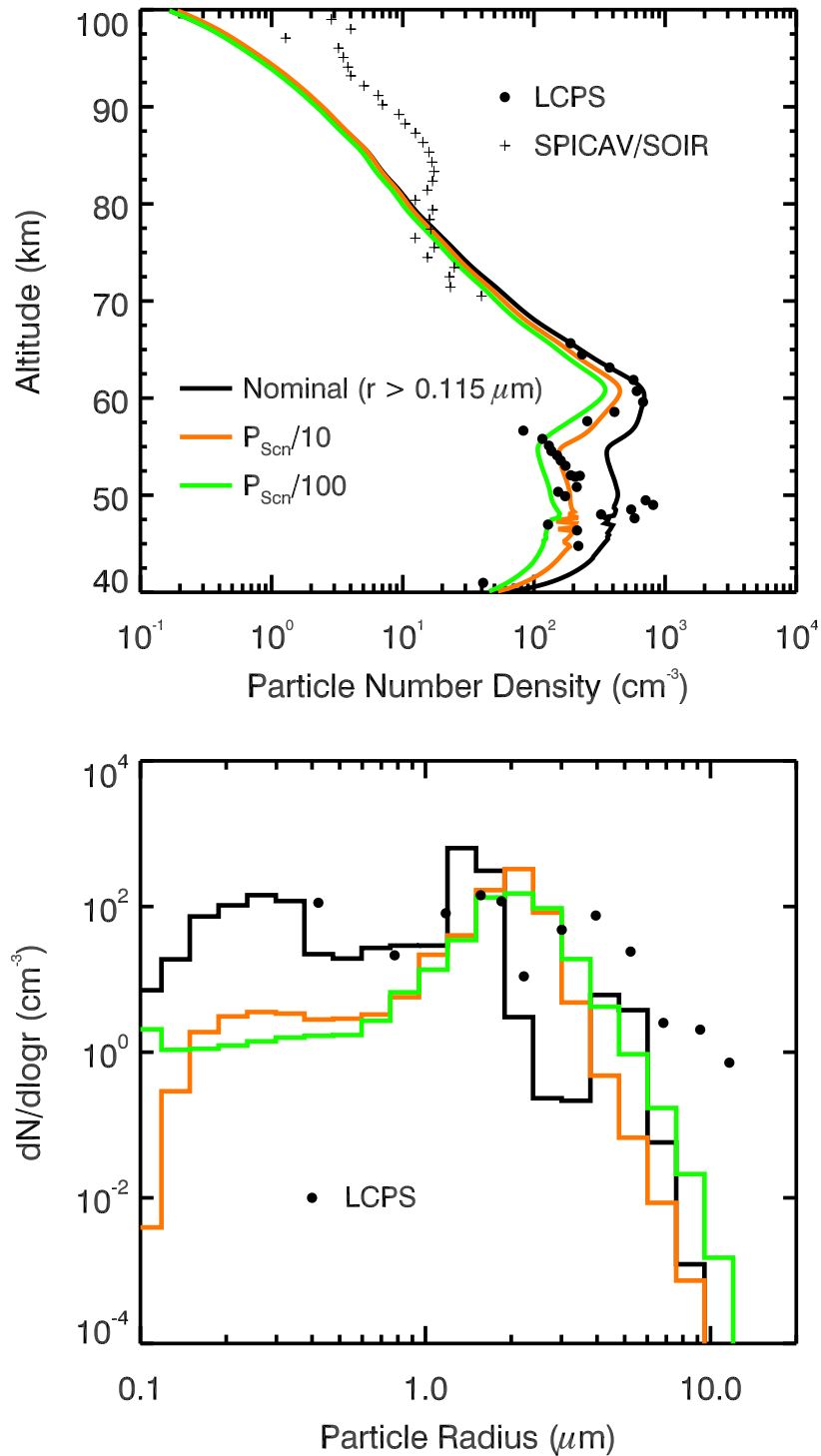
Figure 13. Time evolution of the nominal particle size distribution at 84, 74, 64, and 54 km from  $t = 10^8$  s to  $t = 2 \times 10^8$  s. Note the different number density contour and y axis scale for the 84 km plot. The black regions represent parts of the phase space where  $dN/d\log r < 10^{-7} \text{ cm}^{-3}$  at 74, 64, and 54 km, and  $< 0.1 \text{ cm}^{-3}$  at 84 km.



1162  
 1163  
 1164  
 1165  
 1166  
 1167  
 1168  
 1169  
 1170

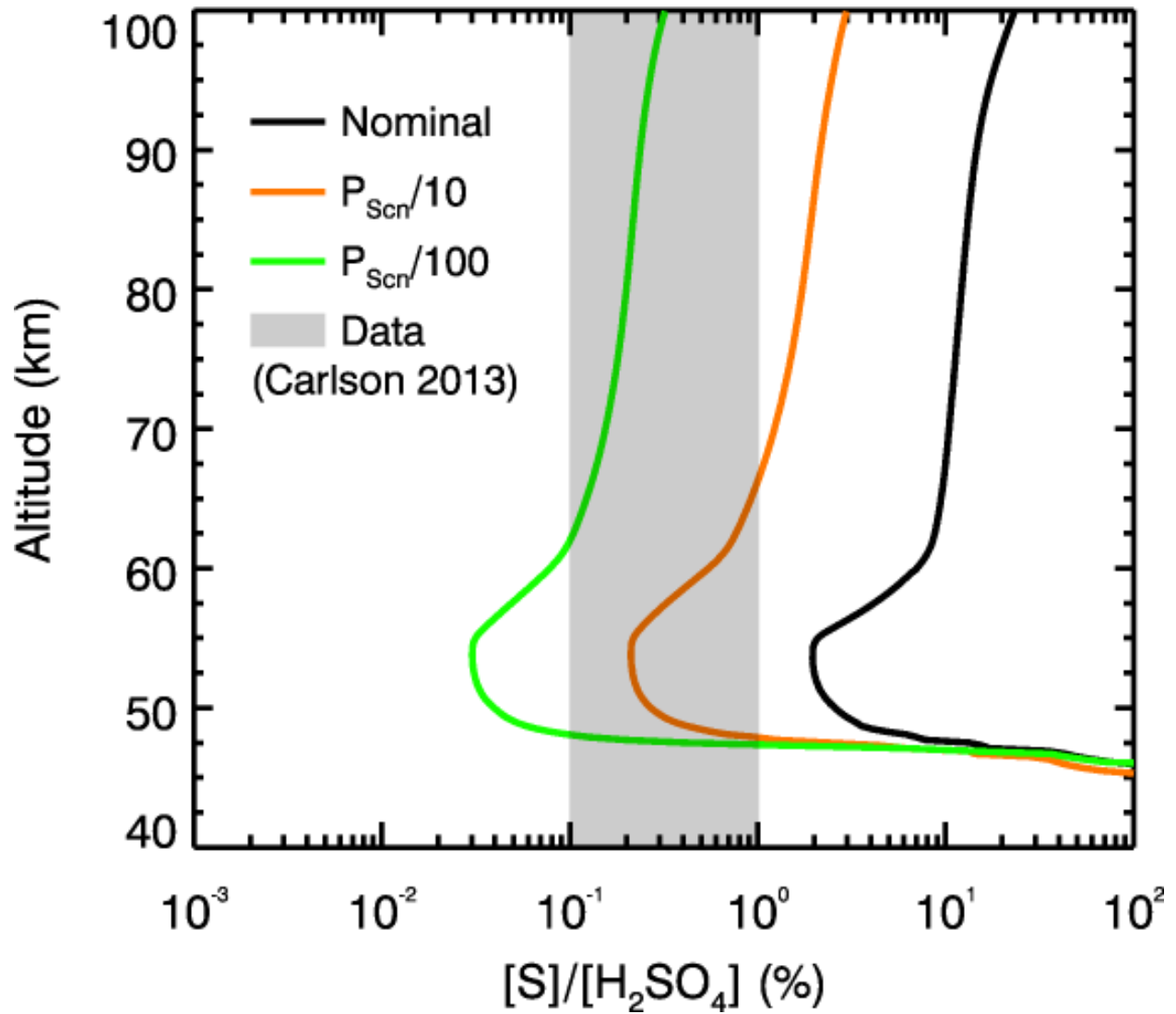
Figure 14. The time evolution of the nominal sulfuric acid vapor (blue) and particle (red) mass fluxes at the bottom of the model domain from  $t = 10^8 \text{ s}$  to  $t = 2 \times 10^8 \text{ s}$  plotted with the average of the total flux during this time period (black), all expressed in units of mass equivalent to  $10^{12}$  sulfuric acid molecules per unit area per second, where each molecule has mass  $M_{SA} \sim 1.6 \times 10^{-22} \text{ g}$ . The negative values indicate downward fluxes.





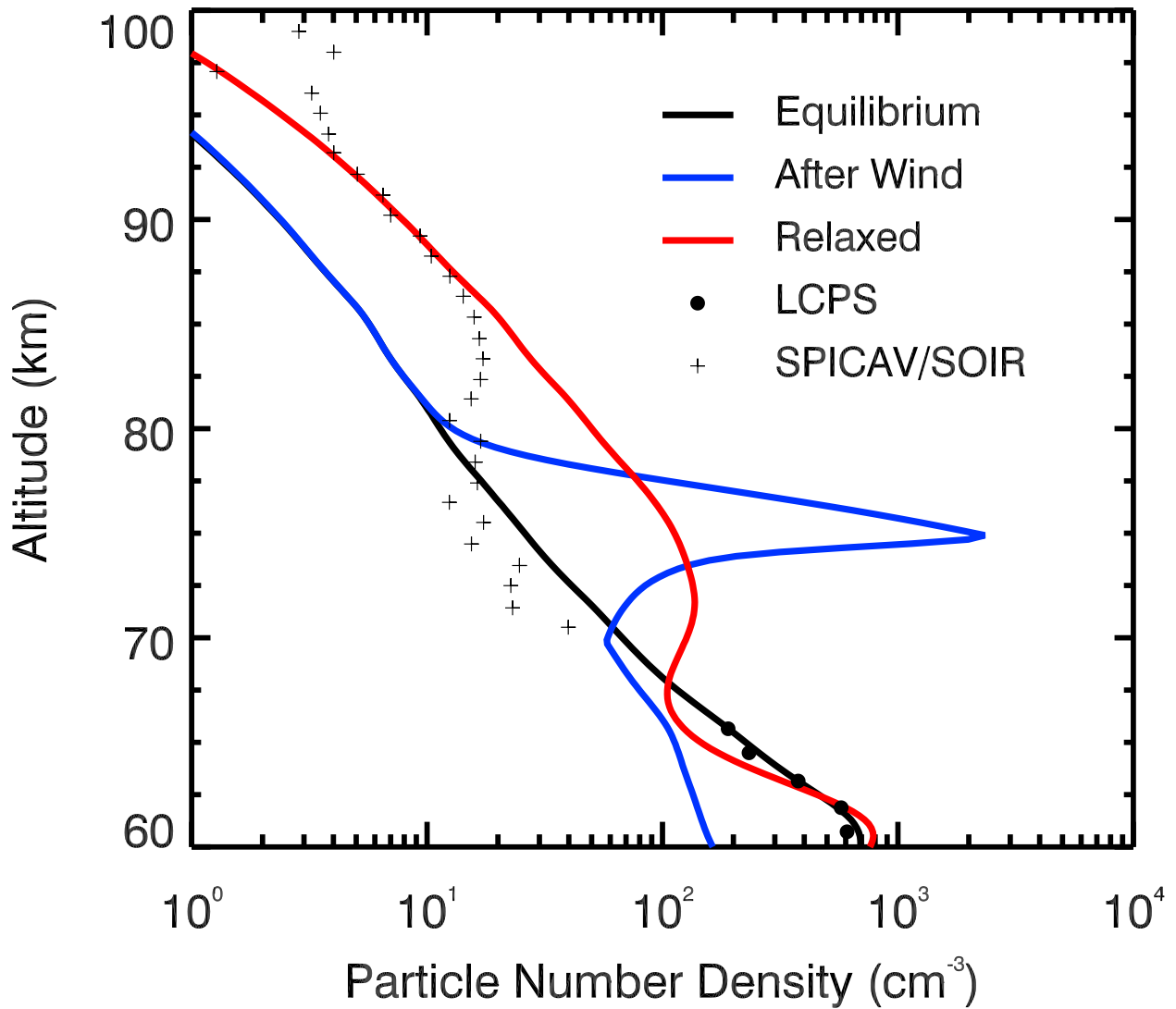
1171  
 1172  
 1173  
 1174  
 1175  
 1176  
 1177  
 1178

Figure 15. The number density (top) and size distribution at 54 km (bottom) of the nominal (black), one order of magnitude reduction in sulfur production (orange), and two orders of magnitude reduction in sulfur production (green) cases. The curves in the top figure are compared to total number density data from LCPS (filled circles) (Knollenberg and Hunten 1980) and Venus Express (pluses) (Wilquet et al. 2009). The histograms in the bottom figure are compared to LCPS size data at 54.2 km (filled circles) (Knollenberg and Hunten 1980).



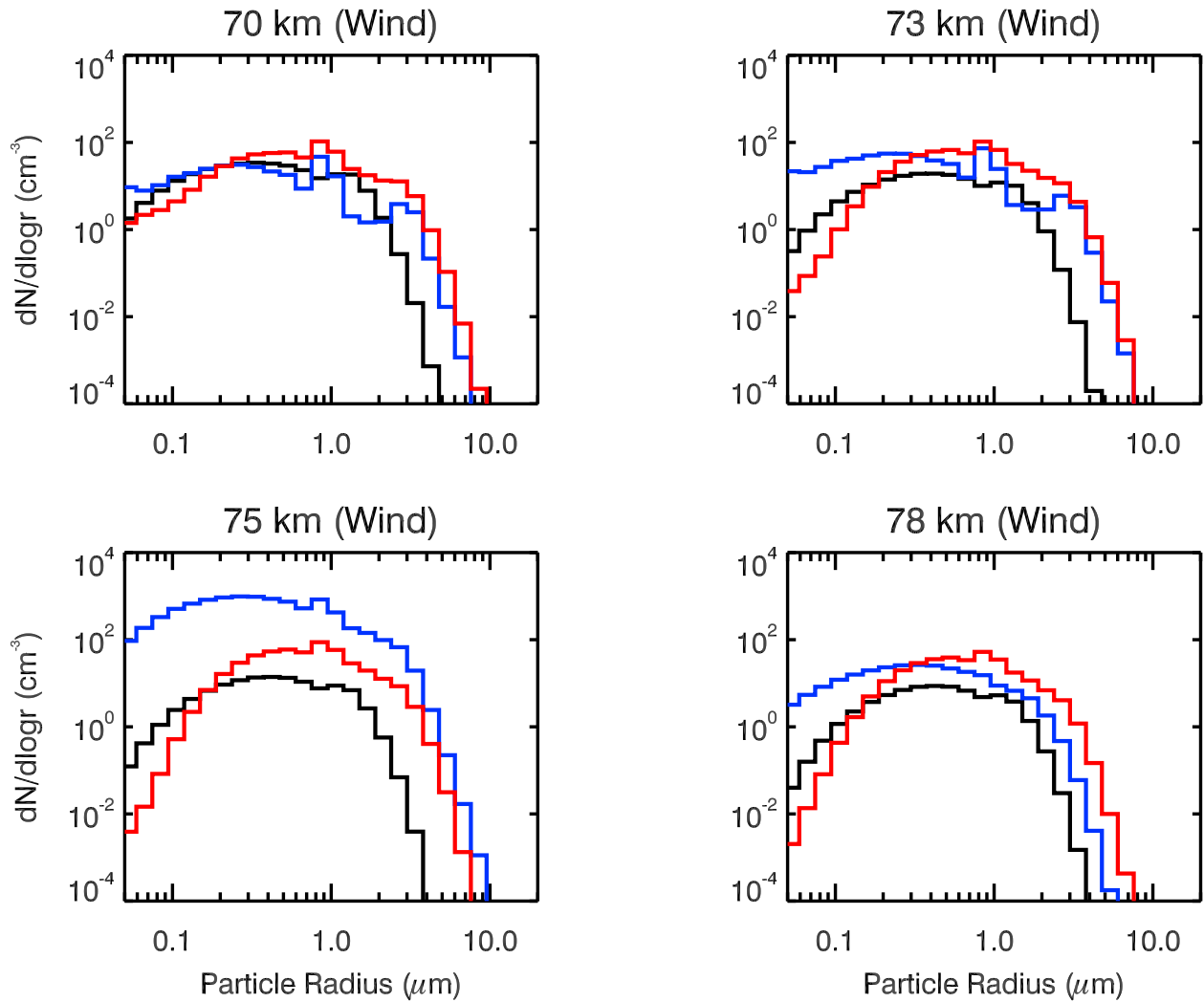
1179  
 1180  
 1181  
 1182  
 1183  
 1184  
 1185  
 1186  
 1187

Figure 16. The average mass ratio of sulfur to sulfuric acid in cloud and haze droplets as a function of altitude for the nominal (black), one order of magnitude reduction in sulfur production (orange), and two orders of magnitude reduction in sulfur production (green) cases. The two red dashed lines show the range of mass ratios as constrained by fits to UV data (Barker et al. 1975) produced by Carlson (2010, revisions via personal communication, Sept. 2<sup>nd</sup>, 2013).



1188  
 1189  
 1190  
 1191  
 1192  
 1193  
 1194  
 1195

Figure 17. Number density profiles of the upper cloud and haze before (black), immediately after (blue), and  $5 \times 10^5$  s after (red) a  $5 \times 10^4$  s transient wind event. The total number density data from LCPS (filled circles) (Knollenberg and Hunten et al. 1980) and Venus Express (pluses) (Wilquet et al. 2009) are plotted for comparison. The wind speed profile is shown in Fig. 6.



1196  
 1197  
 1198  
 1199  
 1200  
 1201

Figure 18. Particle size distribution before (black), immediately after (blue), and  $5 \times 10^5$  s after (red) a  $5 \times 10^4$  s transient wind event, plotted for various altitudes close to the turnover altitude of the transient wind. The wind speed profile is shown in Fig. 6.

1202 Table 1. Model parameters.  
1203

	Nominal Model	Other Values Used
<b>Surface Gravity</b>	887.0 cm s <sup>-2</sup>	
<b>Atmospheric Mole. Wt.</b>	43.45 g mol <sup>-1</sup> (CO <sub>2</sub> )	
<b>Condensable Mole. Wt.</b>	98.08 g mol <sup>-1</sup> (H <sub>2</sub> SO <sub>4</sub> )	
<b>Atmospheric Viscosity<sup>a</sup></b>	1.496 x 10 <sup>-4</sup> g cm <sup>-1</sup> s <sup>-1</sup>	
<b>Sulfuric Acid Surface Tension<sup>b</sup></b>	72.4 erg cm <sup>-2</sup>	
<b>T-P Profile</b>	Figure 1	
<b>Water Vapor Profile</b>	Figure 3	
<b>Production Rates</b>		
Meteoric Dust	4800 cm <sup>-2</sup> s <sup>-1</sup> (Fig. 5)	
Photochemical CNs	1.75 x 10 <sup>6</sup> cm <sup>-2</sup> s <sup>-1</sup> (Fig. 2)	Nominal/10 <sup>c</sup> , Nominal/100 <sup>c</sup>
Sulfuric Acid Vapor	6 x 10 <sup>11</sup> cm <sup>-2</sup> s <sup>-1</sup> (Fig. 2)	
<b>Time Domain</b>		
Time Step	10 s	
Total Simulation Time	2 x 10 <sup>8</sup> s	5 x 10 <sup>4</sup> s <sup>d</sup> , 5 x 10 <sup>5</sup> s <sup>d</sup>
<b>Altitude Domain</b>		
Thickness of Altitude Level	200 m	
Total Altitude Levels	300	
<b>Size Domain</b>		
Mass Ratio Between Bins	2	
Number of Bins	45	
Smallest Bin Size	1.3 nm	
Photochemical CN Size	10.4 nm <sup>e</sup>	
<b>Initial Conditions</b>		
Meteoric Dust	0 cm <sup>-3</sup>	
Photochemical CNs	0 cm <sup>-3</sup>	
Sulfuric Acid Vapor	0 ppm	
<b>Boundary Conditions</b>		
Meteoric Dust (Top)	Zero flux	
Photochemical CNs (Top)	Zero flux	
Sulfuric Acid Vapor (Top)	Zero flux	
Meteoric Dust (Bottom)	0 cm <sup>-3</sup>	
Photochemical CNs (Bottom) <sup>f</sup>	40 cm <sup>-3</sup>	
Sulfuric Acid Vapor (Bottom)	3 ppm	
<b>Wind Speed</b>	0 cm s <sup>-1</sup>	Figure 6 <sup>d</sup>

1204  
1205 <sup>a</sup> Value at 300 K. Viscosity dependence on temperature is calculated using Sutherland's equation  
1206 and parameters from White (1991).  
1207 <sup>b</sup> Value for a flat surface at ~60 km, where temperature ~ 260 K and sulfuric acid weight  
1208 percentage of sulfuric acid droplets ~ 80%.  
1209 <sup>c</sup> See Sec. 3.3.  
1210 <sup>d</sup> For transient wind tests (Sec. 2.6 and 3.4).  
1211 <sup>e</sup> We use 10.4 nm instead of 10 nm as 10.4 nm corresponds to the radius represented by one of  
1212 the discrete size bins in our model (bin 10).

1213 <sup>f</sup> These photochemical CNs have radius  $\sim 0.17 \mu\text{m}$ , consistent with the mean size of the particles  
1214 at  $\sim 40 \text{ km}$  observed by Pioneer Venus LCPS (Knollenberg and Hunten 1980).  
1215